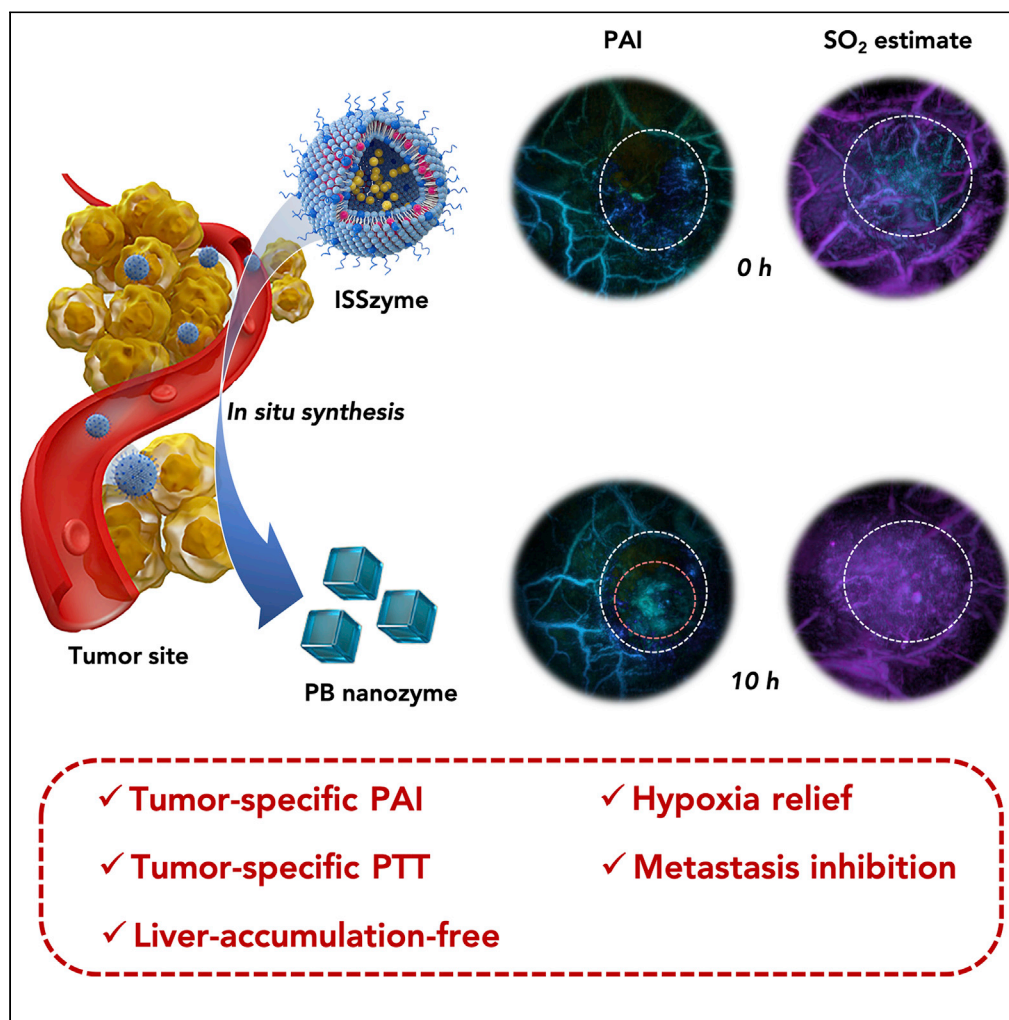


## Article

*In situ* synthesized nanozyme for photoacoustic-imaging-guided photothermal therapy and tumor hypoxia relief

Chaoyi Chen,  
Yuwen Chen,  
Xuanhao Wang, ...,  
Yuan Wang,  
Xiaolong Liang,  
Cheng Ma

xiaolong\_liang@bjmu.edu.cn  
(X.L.)  
cheng\_ma@tsinghua.edu.cn  
(C.M.)

**Highlights**

A new paradigm in nanozyme-based imaging and therapy is demonstrated

PB nanozyme is synthesized *in situ* through the interaction of ISSzyme with GSH

ISSzyme is capable of tumor-specific and liver-accumulation-free PAI and PTT

ISSzyme-induced tumor hypoxia relief is demonstrated by 3D  $SO_2$  estimate

Chen et al., iScience 26,  
106066  
February 17, 2023 © 2023 The  
Authors.  
[https://doi.org/10.1016/  
j.isci.2023.106066](https://doi.org/10.1016/j.isci.2023.106066)

## Article

# *In situ* synthesized nanozyme for photoacoustic-imaging-guided photothermal therapy and tumor hypoxia relief

Chaoyi Chen,<sup>1</sup> Yuwen Chen,<sup>1</sup> Xuanhao Wang,<sup>1</sup> Lulu Zhang,<sup>2</sup> Yan Luo,<sup>1</sup> Qingshuang Tang,<sup>2</sup> Yuan Wang,<sup>2</sup> Xiaolong Liang,<sup>2,\*</sup> and Cheng Ma<sup>1,3,4,\*</sup>

## SUMMARY

Nanozymes have attracted extensive research interest due to their ideal enzymatic catalytic performance; however, uncontrollable activities and nonspecific accumulation limit their further clinical application. To overcome these obstacles, we proposed *in situ* synthesized nanozyme, and realized the concept through an intelligent nanosystem (ISSzyme) based on Prussian blue (PB) precursor. PB nanozyme was synthesized at the tumor sites through the interaction of ISSzyme with glutathione, which was demonstrated by comparing with conventional PB nanozyme. ISSzyme is capable of tumor-specific photoacoustic imaging (PAI) and photothermal therapy (PTT), reducing the false-positive signals of PAI and the treatment side effects of PTT. ISSzyme has catalase-like activities, resulting in tumor hypoxia relief and metastasis inhibition. More importantly, the *in situ* synthesized PB nanozyme has the favorable property of minimal liver accumulation. Considering the above advantages, ISSzyme is expected to shed light on the design of the next-generation artificial enzymes, with many new biomedical applications.

## INTRODUCTION

Nanozymes have attracted extensive research interest in the past decade due to their enzyme-like activities.<sup>1,2</sup> Compared with natural enzymes, nanozymes possess several prominent advantages, including low cost, adjustable catalytic activities, multiple enzyme-like activities, enhanced stability, and robustness toward harsh conditions.<sup>3–5</sup> As a new generation of artificial enzymes, nanozymes have been given great hope for biosensing and biomedical applications, including molecule detection,<sup>6–8</sup> cancer therapy,<sup>6,9–15</sup> antibacterial activity,<sup>16,17</sup> antioxidation,<sup>18,19</sup> inflammation alleviation,<sup>20</sup> hyperuricemia therapy,<sup>21</sup> Parkinson disease therapy,<sup>22</sup> and so on. To distinguish these novel nanomaterials with intrinsic enzyme-like properties from other nanocomplexes, the term “nanozymes” has been introduced. Since the discovery of Fe<sub>3</sub>O<sub>4</sub>-based nanozyme in 2007, many nanomaterials with remarkable enzyme-like activities have been uncovered, such as metal-based nanoparticles,<sup>6–23</sup> rare earth-based nanoparticles,<sup>24,25</sup> graphene oxide nanoparticles,<sup>26</sup> polypyrrole nanoparticles,<sup>27</sup> and so on. However, uncontrollable activities and nonspecific accumulation limit the clinical application of these nanozymes. The off-target activity can backfire on the desired treatment.<sup>28,29</sup> Therefore, nanozymes are required to specifically locate in the target cells. Meanwhile, less than 0.7% of the injected nanoparticles can be delivered to the solid tumor, and most nanoparticles accumulate in metabolic organs independent of the site of injection.<sup>30</sup> This not only leads to low efficiency after systemic administration but also causes damage to normal organs.<sup>31</sup> For instance, nanozymes are still prone to accumulate in the liver, which is rich in phagocytic cells and holes with sizes of 50–200 nm.<sup>32</sup> This inexpectant accumulation not only causes hepatotoxicity and destruction of the redox balance but also has an adverse effect on tumor therapy.<sup>32,33</sup> Moreover, those nanozymes tend to be readily captured by the reticuloendothelial system during blood circulation, potentially generating false signals during diagnosis and causing damage to normal tissues.<sup>31</sup> Therefore, it is urgent to design a controllable nanozyme with high utilization efficiency and biosafety. To solve the limitations mentioned above, our strategy is to develop a nanosystem with tumor-specific response and the ability to synthesize nanozymes *in situ*.

<sup>1</sup>Department of Electronic Engineering, Beijing National Research Center for Information Science and Technology, Tsinghua University, Beijing 100084, China

<sup>2</sup>Department of Ultrasound, Peking University Third Hospital, Beijing 100191, China

<sup>3</sup>Institute for Precision Healthcare, Tsinghua University, Beijing 100084, China

<sup>4</sup>Lead contact

\*Correspondence: [xiaolong\\_liang@bjmu.edu.cn](mailto:xiaolong_liang@bjmu.edu.cn) (X.L.), [cheng\\_ma@tsinghua.edu.cn](mailto:cheng_ma@tsinghua.edu.cn) (C.M.)

<https://doi.org/10.1016/j.isci.2023.106066>



Prussian blue (PB) has been widely investigated as a nanozyme with excellent electrochemical and optical properties.<sup>34</sup> PB nanoparticles have been approved as an antidote for treatment of internal radioactive contamination with thallium and cesium by the United States Food and Drug Administration.<sup>35</sup> In addition, PB nanoparticles can be modified to achieve a variety of functions, for example, it can be used as drug carriers to improve the therapeutic efficacy.<sup>35–38</sup> Due to the reduction ability and low redox potential of PB nanoparticles, PB nanozyme has strong antioxidant activities, including peroxidase-like activities, catalase-like activities, and superoxide dismutase-like activities, which are very important for regulating oxidative stress in various diseases.<sup>36,39</sup> PB nanozyme can decompose  $H_2O_2$  in tumor sites to produce  $O_2$ , so as to relieve tumor hypoxia and inhibit tumor metastasis.<sup>34,40</sup> Meanwhile, PB nanozyme can remove excess reactive oxygen species (ROS) from the body to treat ROS-related diseases.<sup>41</sup> Moreover, PB nanoparticles have been widely used as photothermal agents for photothermal therapy (PTT) due to its excellent near-infrared (NIR) absorption and photothermal conversion efficiency.<sup>34,38</sup> More importantly, PB nanozyme has been demonstrated to simultaneously relieve inflammation caused by hyperthermia during PTT, thanks to its antioxidative catalytic activity.<sup>42</sup> However, the PB functions are not tumor specific and are therefore “always on”, inducing undesirable side effects during PTT and generating interfering background signals during imaging.

In recent years, photoacoustic (PA) imaging (PAI) has been developed for tumor imaging.<sup>43,44</sup> It employs non-ionizing light excitation and ultrasound detection to obtain high spatial resolution, deep penetration, and rich contrast.<sup>45–48</sup> Label-free PA imaging can be used for the imaging of endogenous chromophores such as hemoglobin,<sup>49,50</sup> lipids,<sup>51,52</sup> and melanin,<sup>48,53</sup> while additional contrasts can be obtained by introducing exogenous agents. Nanomaterials have been employed as exogenous PA contrast agents, such as NIR dyes,<sup>54–58</sup> carbon nanomaterials,<sup>59,60</sup> semiconducting polymer nanoparticles,<sup>61,62</sup> and metallic nanoparticles.<sup>63,64</sup> These agents can provide outstanding contrasts for target molecules that are otherwise invisible. For example, tumors can be labeled with externally administered contrast agents, either by the enhanced permeability and retention (EPR) effect or active targeting.<sup>65,66</sup> However, intrinsic tissue chromophores inevitably generate a strong PA background, which tends to reduce or even overwhelm the contrast from the contrast agents.<sup>67,68</sup> For example, the liver suffers from such intrinsic background due to its strong optical absorption. Moreover, similar to the photothermal agents, traditional PA contrast agents whose absorption spectra stay unchanged (we also refer to such agents as “always on”) suffer from false-positive signals during disease diagnosis.<sup>6,69</sup> Therefore, it is a widely used strategy to design PA contrast agents that exhibit specific, switchable response to the tumor. Among those specific physiological signals in the tumor microenvironment (TME), glutathione (GSH), the most abundant endogenous active small molecular in cells and tissues, plays an important role in life activities and in maintaining the redox balance, while the concentration of GSH in cancer cells is 2–20 mM, three orders of magnitude higher than that in normal cells.<sup>63,70–74</sup>

Herein, we demonstrate a new paradigm in nanozyme-based imaging and therapy in which the nanozyme is synthesized *in situ* through an intelligent nanosystem (ISSzyme) based on PB precursors (Figure 1). ISSzyme exhibits high sensitivity and specificity to GSH, a chemical highly expressed at the tumor site as a biomarker for cancer. The nanosystem can synthesize PB nanozyme *in situ* by interacting with GSH, which was demonstrated by comparing with control experiments using the conventional PB nanozyme. The strong NIR absorption of the PB nanozyme endows ISSzyme with the capability of tumor-specific PAI and PTT, giving rise to reduced false-positive signals in PAI and less side effects in PTT. More importantly, the PB nanozyme synthesized *in situ* has a “liver-accumulation-free” property that not only reduces the damage to the liver and other metabolic organs but also makes the imaging of tumors embedded in a strong intrinsic tissue background possible. In addition, the *in situ* synthesized PB nanozyme shows catalase-like activities and can decompose  $H_2O_2$  in the tumor site to produce  $O_2$ , resulting in tumor hypoxia relief and metastasis inhibition. To the best of our knowledge, this is the first time to propose and achieve synthesized nanozymes *in situ*. Thus, we anticipate that the concept of ISSzyme may shed light on the design of the next-generation artificial enzymes and PA agents, with many new biomedical applications.

## RESULTS

### Preparation and *in vitro* characterization of ISSzyme

The ISSzyme was prepared following an ethanol injection method and assembled from potassium ferrocyanide, iron tri (acetylacetonate), DSPC, and DSPE-PEG2000, resulting in good water dispersibility.<sup>75</sup> The transmission electron microscopy (TEM) image showed that the as-prepared ISSzyme exhibited spherical

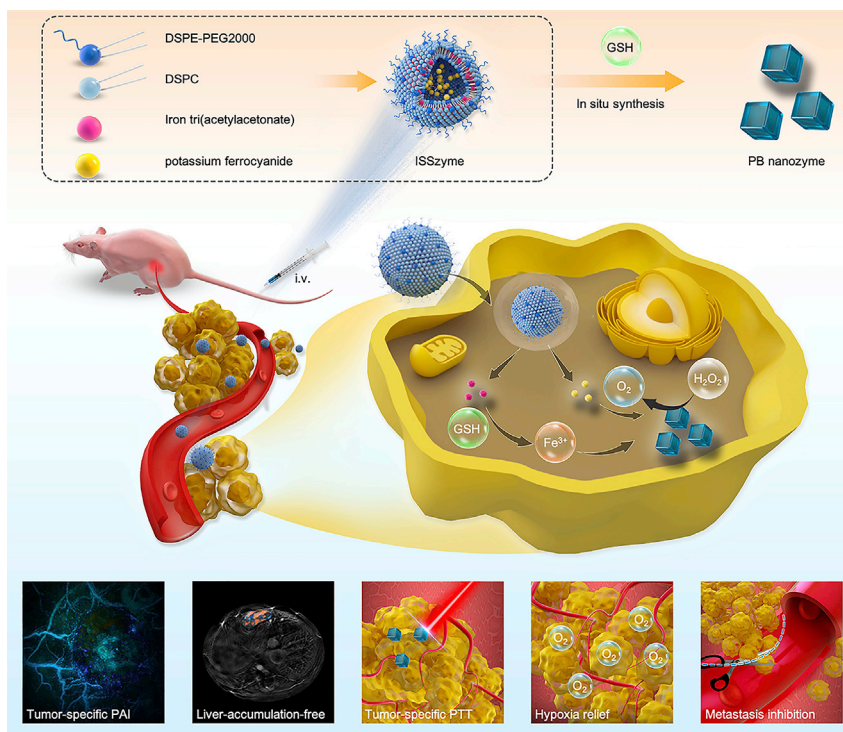


**Figure 1. Schematic illustration of the mechanism of ISSzyme for tumor-specific PAI-guided PTT and tumor hypoxia relief**

morphology with an average diameter of  $56 \pm 3$  nm (Figure 2A). While, the GSH-treated ISSzyme exhibited cubic morphology with an average size of  $57 \pm 7$  nm and characterized by TEM (Figure 2B). Energy-dispersive X-ray spectroscopic elemental mapping showed the distribution of Fe, K elements in the ISSzyme with or without GSH co-incubation, indicating the successful encapsulation of potassium ferrocyanide and iron tri (acetylacetonate) (Figure 2C). Meanwhile, the hydrodynamic size and the zeta potential of ISSzyme in aqueous solutions were  $72 \pm 3$  nm (Figure S1) and  $-15 \pm 9$  mV (Figure S2), determined by the dynamic light scattering measurement, indicating that ISSzyme could effectively accumulate in tumors via the EPR effect due to their suitable particle sizes and a negative zeta potential. To investigate the GSH responsiveness of ISSzyme, GSH of different concentrations (0–8 mM) was added into ISSzyme solutions (Figure 2D). The spectra of the mixed solutions exhibited broad absorption in the 600–900 nm spectral range with an absorption peaked at  $\sim 700$  nm, and the absorbance increased with GSH concentration (Figure 2E). The ratio between the absorbance of the ISSzyme solutions at 700 nm and 990 nm ( $Abs_{700}/Abs_{990}$ ) increased linearly with GSH concentration in the range of 0.5–6 mM (Figure 2F). The change of absorption spectra might be due to the substitution of acetylacetonate ligand of iron tri (acetylacetonate) by the GSH molecule, resulting in the production of free iron (III). Subsequently, iron (III) reacted with potassium ferrocyanide to produce a stable PB nanozyme. At the saturation point,  $Abs_{700}/Abs_{990}$  ( $2.69 \pm 0.03$ ) was 4.14 times that of zero concentration ( $0.65 \pm 0.02$ ). The spectral change indicated that ISSzyme could generate PB nanozyme under the action of GSH, which was also validated by comparing with the TEM images (Figure S3) and the hydrodynamic size (Figure S4). In addition, the process of generating PB nanozymes in response to GSH was very rapid (Figure S5), and can also be carried out under weak acidic and neutral conditions (Figure S6).

The significant absorbance of PB nanozyme in the NIR region gives GSH-treated ISSzyme the potential for PAI. *In vitro* PA images of ISSzyme solutions with various GSH concentration were recorded at 700 and 990 nm, and the images were displayed in pseudocolor (green for 700 nm and red for 990 nm). As the GSH concentration increased, the PA amplitude of ISSzyme at 700 nm also increased in proportion, whereas the PA amplitude at 990 nm remained nearly unchanged (Figure 2G). This enabled us to perform ratiometric PA imaging of GSH using two wavelengths: the ratio between the PA amplitudes at 700 nm and 990 nm ( $PA_{700}/PA_{990}$ ) increased from  $10 \pm 3$  (zero concentration) to a saturated value of  $48.7 \pm 0.9$ ,

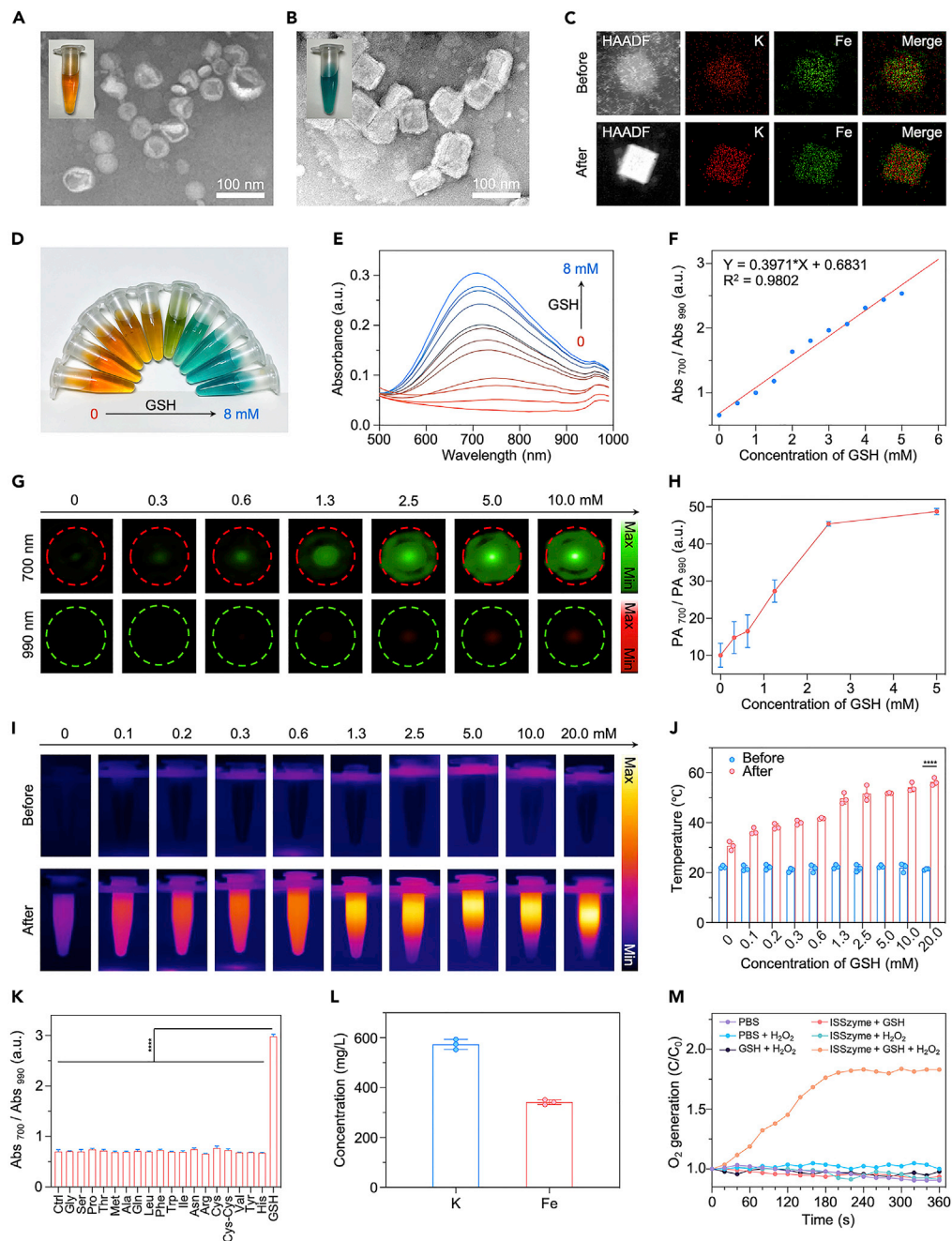


**Figure 2. Characterization of ISSzyme**

(A and B) Representative TEM of ISSzyme (A) and ISSzyme treated with GSH (B).  
 (C) EDS elemental mapping of K and Fe in ISSzyme before and after GSH co-incubation.  
 (D) Photograph of ISSzyme solution after addition of GSH (0–8 mM, 5 min).  
 (E) UV–vis absorption spectra of ISSzyme upon addition of GSH at different concentrations.  
 (F) Ratiometric absorption signals of ISSzyme ( $Abs_{700}/Abs_{990}$ ) as a function of GSH concentrations.  
 (G) PA images of ISSzyme in the presence of GSH at different concentrations. The samples were recorded at 700 and 990 nm, which were indicated in green and red, respectively.  
 (H) Quantification of the ratiometric PA signals ( $PA_{700}/PA_{990}$ ) of ISSzyme as a function of GSH concentration.  
 (I) *In vitro* IR thermal images of ISSzyme incubated with GSH (from 0 to 20 mM) before and after irradiation (808 nm,  $0.8 \text{ W cm}^{-2}$ , 5 min).  
 (J) Temperature ( $^{\circ}\text{C}$ ) as a function of GSH concentration.  
 (K)  $Abs_{700}/Abs_{990}$  as a function of amino acid concentration.  
 (L) Concentration (mg/L) of K and Fe.  
 (M)  $\text{O}_2$  generation ( $C/C_0$ ) as a function of time (s) for different conditions: PBS, PBS +  $\text{H}_2\text{O}_2$ , GSH +  $\text{H}_2\text{O}_2$ , ISSzyme + GSH, ISSzyme +  $\text{H}_2\text{O}_2$ , and ISSzyme + GSH +  $\text{H}_2\text{O}_2$ .

**Figure 2. Continued**

(J) Corresponding photothermal heating statistics of (I).

(K) Ratiometric absorption signals of ISSzyme ( $Abs_{700}/Abs_{990}$ ) in the absence (control) or presence of different amino acids (10 mM).

(L) ICP-OES measurement of ISSzyme.

(M) Time course of  $O_2$  evolution of ISSzyme with different treatment.

exhibiting a 4.87-fold increase (Figure 2H). To evaluate the *in vitro* photothermal capability, ISSzyme solutions treated by various concentration of GSH were irradiated by a NIR laser (808 nm,  $1\text{ W cm}^{-2}$ ) for 10 min, and the ISSzyme solution without GSH co-incubation was used as a control (Figure 2I). Infrared (IR) thermal images were recorded for temperature measurement. The temperature before and after NIR laser irradiation was recorded (Figure 2J). For the GSH-treated samples, the temperature increase after the laser irradiation was obviously related to the GSH concentration. At the saturation point, the temperature after irradiation ( $54.17^\circ\text{C}$ ) was 2.47 times that of before irradiation ( $21.97^\circ\text{C}$ ), while the temperature of the control showed very little change after the irradiation. Moreover, the ISSzyme after GSH treatment exhibited superior photothermal stability (Figure S7) and high photothermal conversion efficiency ( $\eta = \sim 70.9\%$ ), while the ISSzyme without GSH treatment exhibited extremely low photothermal conversion efficiency ( $\eta = \sim 2.3\%$ ). In addition, the ISSzyme's specificity to GSH was evaluated by incubating ISSzyme with 18 kinds of common amino acids. At the saturation point,  $Abs_{700}/Abs_{990}$  ( $2.98 \pm 0.04$ ) of the GSH-treated group showed a 4.3-fold increase, while the other groups showed negligible changes (Figure 2K).

The loading efficiencies of potassium ferrocyanide and iron tri (acetylacetonate) were determined to be about 12.3% and 8.1%, respectively, as determined by inductively coupled plasma optical emission spectrometry (Figure 2L). Considering that the concentration of GSH in cancer cells is much higher than that of normal cells (up to three orders of magnitude increase), ISSzyme can serve as a highly sensitive and specific agent for PAI-guided PTT.<sup>70,74</sup> Moreover, by comparing with the standard absorbance of PB nanozyme at 700 nm, the as-prepared ISSzyme could form approximately  $340\ \mu\text{g mL}^{-1}$  of PB nanozyme after incubation with 5 mM GSH (Figure S8). The leakage of Fe as well as the hydrodynamic size of ISSzyme at different time points indicated that ISSzyme had good stability (Figures S9 and S10). In view of the catalase-like function of ISSzyme and the high  $H_2O_2$  concentration in the TME, ISSzyme was expected to catalyze  $H_2O_2$  to produce  $O_2$ , so as to achieve tumor hypoxia relief.<sup>35,39</sup> The  $O_2$  generation capability of ISSzyme was demonstrated by comparing the dissolved oxygen in solutions with different treatment, including PBS (pH = 6.5), PBS +  $H_2O_2$ , GSH +  $H_2O_2$ , ISSzyme + GSH, ISSzyme +  $H_2O_2$ , and ISSzyme + GSH +  $H_2O_2$ .  $O_2$  was rapidly produced only in the sample with both GSH-treated ISSzyme and  $H_2O_2$ , while the dissolved oxygen of other groups showed negligible changes (Figure 2M).

***In vitro* ISSzyme-mediated cytotoxicity and hypoxia relief profiles**

PB nanozyme is an efficacious PTT agent due to its excellent photothermal properties;<sup>34,40</sup> therefore, ISSzyme in the presence of GSH is well suited for tumor-specific PTT. Before studying the anticancer and hypoxia relief effect of ISSzyme *in vitro*, its biocompatibility was investigated. To this end, ISSzyme was co-incubated with human umbilical vein endothelial cells (HUVEC) or murine mammary carcinoma 4T1 cells at different concentrations (Figure S11). The cellular viabilities were detected via a thiazolyl blue tetrazolium bromide (MTT) assay after 24 h of co-incubation with ISSzyme. No obvious cytotoxicity was observed in both 4T1 cells and HUVECs, preliminarily showing good biocompatibility of ISSzyme. PTT-induced cytotoxicity was investigated quantitatively by the MTT assay. First of all, 4T1 cells were treated with ISSzyme in gradient concentrations and irradiated by a NIR laser (808 nm,  $1\text{ W cm}^{-2}$ , 5 min), while the group without ISSzyme treatment and irradiation was used as a control. The cell viabilities gradually decreased with the increase in ISSzyme concentration (Figure 3A). When the concentration of ISSzyme reached  $200\ \mu\text{g mL}^{-1}$ , the cell viability of 4T1 cells decreased to 8.54% after irradiation, which was one-tenth of that without irradiation. Subsequently, the cell viabilities of ISSzyme-treated ( $100\ \mu\text{g mL}^{-1}$ ) 4T1 cells with different irradiation conditions (power density: 0.5, 1.0, 1.5, and  $2.0\text{ W cm}^{-2}$ , time: 0, 3, 5, and 7 min) were measured (Figure 3B). The results showed that cell viability was negatively correlated with the power density and irradiation time, demonstrating the fast and stable photothermal conversion of GSH-treated ISSzyme. The anticancer ability of ISSzyme *in vitro* was evaluated through both MTT assay and living and dead cell staining. The anticancer abilities of irradiation treatment (808 nm,  $1\text{ W cm}^{-2}$ , 5 min) and treatment of ISSzyme ( $100\ \mu\text{g mL}^{-1}$ ) were demonstrated separately. MTT assay results showed that either irradiation treatment or ISSzyme treatment alone did not have anticancer ability, but when they were combined,

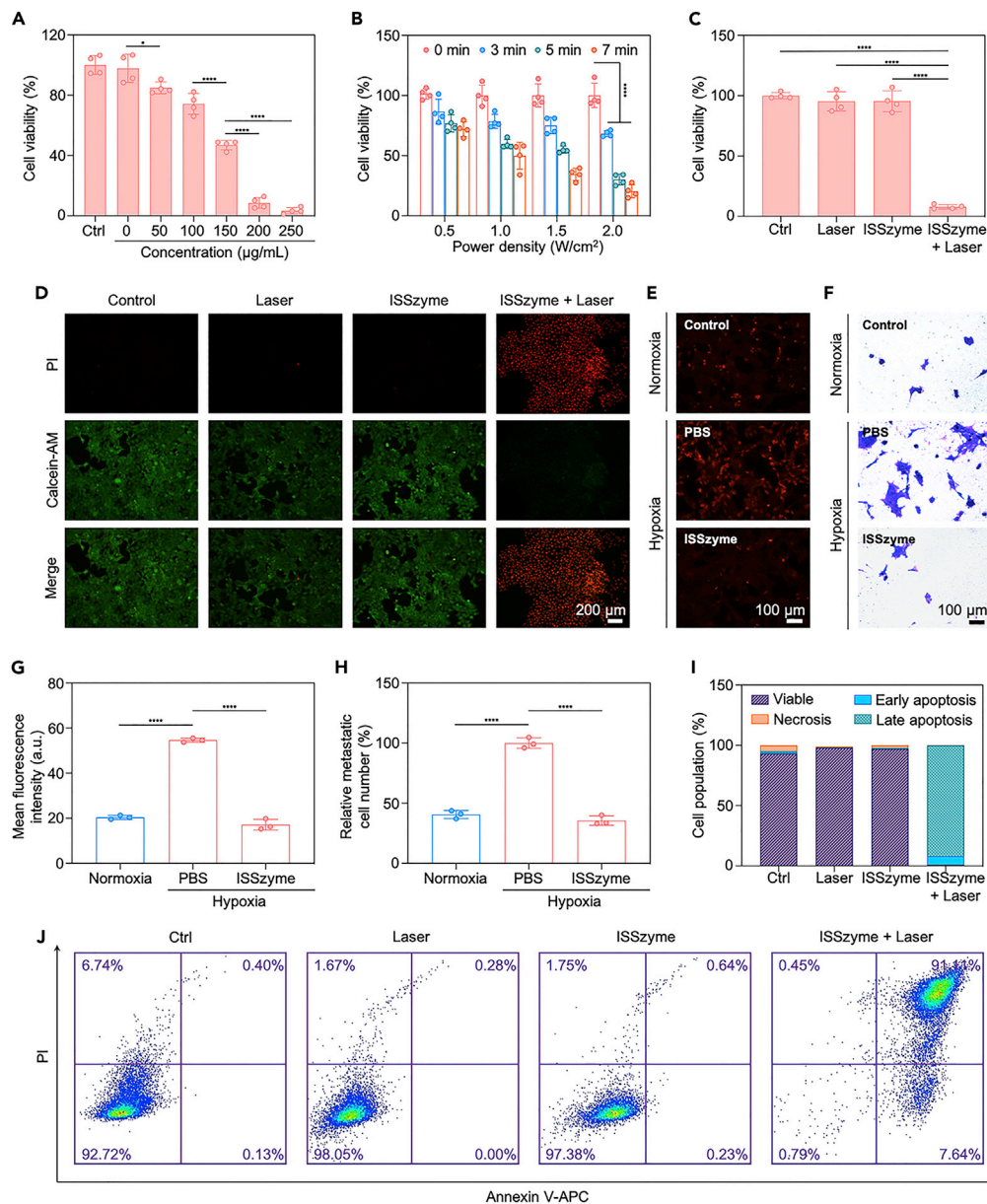


**Figure 3. In vitro ISSzyme-mediated cytotoxicity and hypoxia relief**

(A) Viability of 4T1 cells after incubation with gradient concentrations of ISSzyme and treatment with NIR irradiation (n = 4).  
 (B) Viability of 4T1 cells after incubation with ISSzyme under different irradiation conditions (n = 4).  
 (C and D) Viability (C) and calcein-AM/PI staining (D) of 4T1 cells with different treatments (ISSzyme/PBS, with/without irradiation, n = 4).  
 (E) Fluorescence images of [Ru(dpp)<sub>3</sub>]Cl<sub>2</sub> in 4T1 cells after different treatments (ISSzyme/PBS, hypoxic/normoxia, n = 4).  
 (F) Transwell assay of invasion ability of 4T1 tumor cells.  
 (G) Quantification of [Ru(dpp)<sub>3</sub>]Cl<sub>2</sub> in 4T1 cells after different treatments.  
 (H) Quantification of the relative metastasis number of 4T1 cells after different treatments.  
 (I) Quantitative analysis of flow cytometric apoptosis/necrosis of 4T1 cells with different treatments.  
 (J) Flow cytometric apoptosis/necrosis analysis based on Annexin V-APC/PI staining assay of 4T1 cells after different treatments.

the cell viability decreased significantly (Figure 3C). The living and dead cell staining with calcein-AM and propidium iodide (PI) also proved the efficient PTT of ISSzyme (Figure 3D). Furthermore, the apoptosis characteristics of 4T1 cells after different treatments were studied by flow cytometry (Figures 3I and 3J).

All cells were labeled with Annexin V-APC/PI apoptosis kit after treatment. The group treated with both ISSzyme and irradiation displayed the highest apoptosis, and most cells appeared in the late apoptotic area. In contrast, apoptosis in other groups was almost negligible, and most cells appeared in the viable area. These results identified that the cytotoxicity was mainly associated with apoptosis.

Due to the catalase-like activity, ISSzyme could rapidly induce the decomposition of  $H_2O_2$  into  $O_2$ , so as to alleviate tumor hypoxia.<sup>76</sup> The intracellular  $O_2$  generation capability of ISSzyme was analyzed by an intracellular  $O_2$ -level indicator  $[Ru(dpp)_3]Cl_2$ . When the intracellular  $O_2$  level is low,  $[Ru(dpp)_3]Cl_2$  has significant red fluorescence; when the intracellular  $O_2$  level increases, the red fluorescence will be quenched. Under hypoxic conditions, 4T1 cells with ISSzyme treatment showed extremely weak fluorescence, while 4T1 cells with PBS (PBS, pH = 7.4) appeared fluorescent (Figure 3E). Meanwhile, the fluorescence intensity of the positive control (under normoxia conditions, PBS-treated) was similar to that of the ISSzyme-treated hypoxic group. More quantitatively, the mean fluorescence intensity of PBS-treated hypoxic group ( $54.63 \pm 0.91$ ) was 3.19-fold higher than that of the ISSzyme-treated hypoxic group ( $17.13 \pm 2.42$ ) and 2.67-fold higher than that of the positive control ( $20.43 \pm 0.90$ ), verifying the generation of  $O_2$  from ISSzyme (Figure 3G). The decreased cellular oxygenation can result in the upregulated expression level of HIF- $\alpha$ , which correlates with tumor metastasis and can be downregulated by relieving tumor hypoxia. In order to verify the ability of ISSzyme to inhibit tumor metastasis by relieving tumor hypoxia, the cell invasion ability was measured by a transwell experiment. According to the crystal violet fluorescence image, the density of the 4T1 cells in the PBS-treated hypoxic group was higher, indicating that the tumor cells cultured under hypoxia had higher invasiveness, while the densities of the 4T1 cells in the ISSzyme-treated hypoxic group and the positive control group were lower (Figure 3F). Compared with the PBS-treated hypoxic group, the relative metastatic cell number of the ISSzyme-treated hypoxic group was only 35.59%, while that in the positive control group was 40.68% (Figure 3H). The above results demonstrated that ISSzyme can relieve tumor hypoxia and inhibit tumor metastasis by producing  $O_2$  *in situ*.

### **In situ ISSzyme-assisted PAI of tumor**

*In vivo* biocompatibility of ISSzyme was evaluated before *in vivo* PAI by hematology analysis, blood biochemistry, and histological examination. After intravenous injection of ISSzyme ( $13 \text{ mg kg}^{-1}$ ,  $n = 3$ ), the main parameters of blood biochemistry and hematology, including white blood cell counts, red blood cell counts, hemoglobin, granulocyte percentage, mean corpuscular hemoglobin concentration, mean platelet volume, hematocrit, mean corpuscular volume, platelets, lymphocyte percentage, monocyte percentage, and red blood cell distribution width, exhibited no obvious abnormalities on day 1, 7, and 14 compared with those of the control group (Figure S12). Moreover, the histological examination of major organs (heart, liver, spleen, lung, and kidney) in mice treated with ISSzyme and sampled on days 1, 7, and 14 revealed no apparent histopathological abnormalities or lesions (Figure S13). Thus, our results demonstrated that there were no apparent toxicities induced by ISSzyme at the tested conditions *in vivo*. In order to study the metabolism of ISSzyme *in vivo*, the main organs of mice treated with Cy5.5-labeled ISSzyme at different time points were recorded *ex vivo* by fluorescence imaging (Figure S14). The results (Figure S15) showed that the ISSzyme concentration in each organ reached the peak at 4 h, then the ISSzyme concentration began to decline; ISSzyme was mainly metabolized through the liver. In addition, the feces and urine of mice before and 1 to 10 days after the ISSzyme treatment were collected. The analysis of the Fe content in these feces and urine indicated that the enrichment of ISSzyme in feces was evidently observed compared to that in urine, revealing that ISSzyme was mainly metabolized out of the body through the liver (Figure S16), according to the reported method.<sup>77,78</sup> Moreover, the ISSzyme delivery efficiency to the tumor site was studied quantitatively, indicating that  $\sim 12.3 \text{ ID\%/g}$  of ISSzyme could reach the tumor site after intravenous injection (Figure S17).

The PAI capability of ISSzyme was first validated by intratumoral injection experiments. Two 4T1 xenograft tumors ( $n = 3$ ) were implanted subcutaneously on the back of BALB/c mice in the same transverse plane. One tumor was injected with ISSzyme ( $50 \mu\text{L}$ ,  $2 \text{ mg mL}^{-1}$ ), whereas the other one was injected with PBS ( $50 \mu\text{L}$ ) as the control. After injection, PA images were recorded at different times at 700 and 990 nm using a homemade PA computed tomography (PACT) system (Figures 4A and S18). More quantitatively, the signal in the ISSzyme-treated tumors increased significantly over time; at 6 h post-injection, the value of  $PA_{700}/PA_{990}$  ( $11.6 \pm 0.4$ ) grew 1.53 times compared to the value at 0.5 h ( $7.6 \pm 0.3$ ), while  $PA_{700}/PA_{990}$  of the PBS-treated tumors remained nearly unchanged (Figure 4B).  $PA_{700}/PA_{990}$  of the ISSzyme-treated tumors at 6 h ( $11.6 \pm 0.4$ ) was 1.49-fold higher than the PBS-treated tumors ( $7.8 \pm 0.1$ ). To further prove

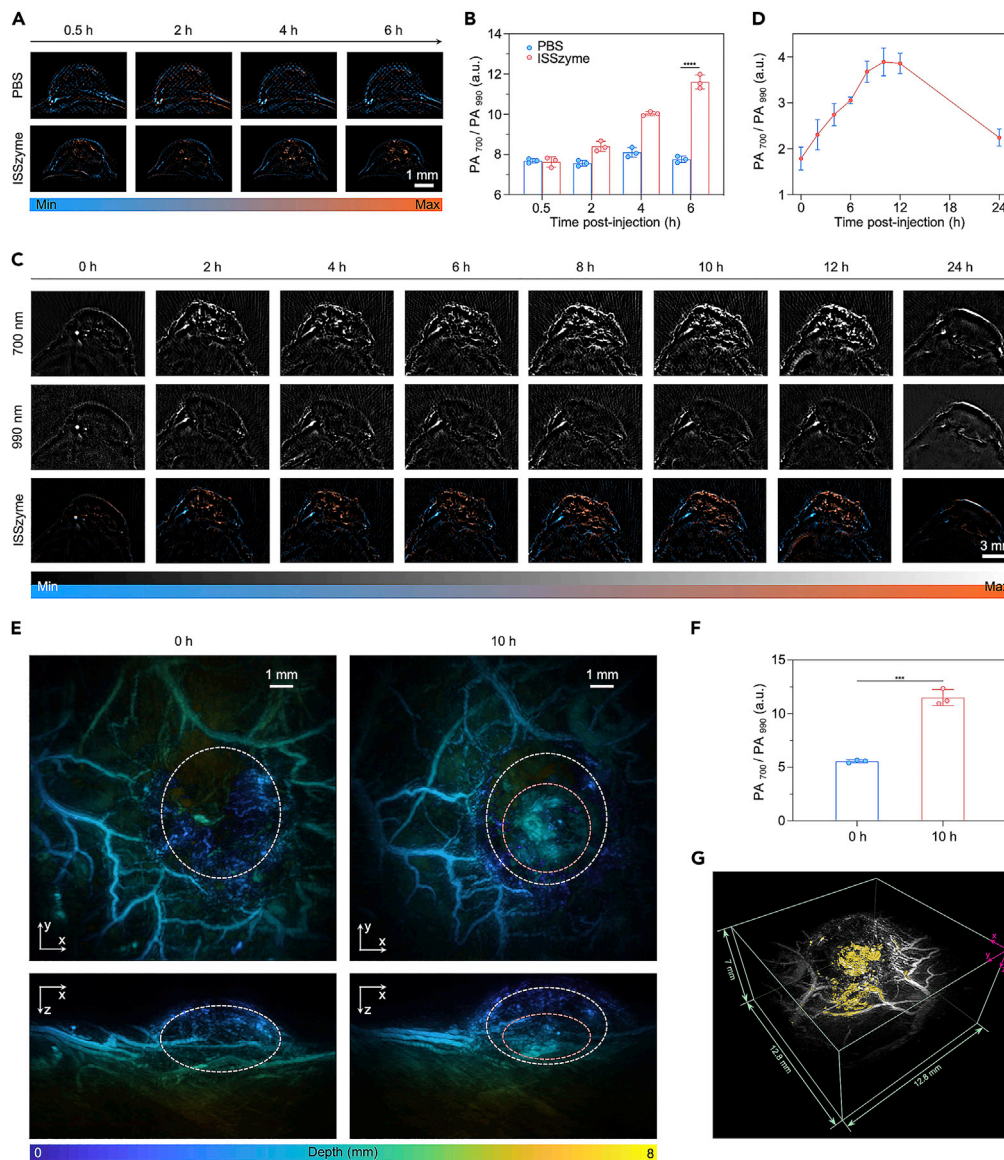


**Figure 4. ISSzyme-assisted tumor PAI *in situ***

(A) Representative PA images of 4T1 tumor-bearing BALB/c mice at 0.5, 2, 4, and 6 h after intratumor administration of PBS and ISSzyme.

(B) Quantification of PA<sub>700</sub>/PA<sub>990</sub> as a function of time post-injection of PBS or ISSzyme (n = 3).

(C) Representative PA images of 4T1 tumor-bearing BALB/c mice before and 2, 4, 6, 8, 10, 12, and 24 h after intravenous administration of ISSzyme.

(D) Quantification of PA<sub>700</sub>/PA<sub>990</sub> as a function of time post-injection of ISSzyme (n = 3).

(E) Horizontal and vertical MIP of representative *in vivo* PAME imaging (700 nm) results of 4T1 tumor-bearing BALB/c mice before and at 10 h post-injection of ISSzyme; white dashed: tumor, red dashed: ISSzyme.

(F) Quantification of PA<sub>700</sub>/PA<sub>990</sub> of tumor site before and after systemic administration.

(G) Spatial distribution of ISSzyme in tumor via PAME, the contrast provided by the ISSzyme was pseudo-colored yellow; see [Video S1](#) for video presentation.

the capability of ISSzyme for *in situ* PAI, systemic administration of ISSzyme (13 mg kg<sup>-1</sup>, n = 3) was carried out, where we imaged the subcutaneous 4T1 xenograft tumor model using PACT (Figure 4C). PAI achieved the ideal results and reached the maximum PA amplitude in the tumor sites at 700 nm at about 10 h post-injection. At this time point, PA<sub>700</sub>/PA<sub>990</sub> (3.9 ± 0.3) was 2.17-fold higher than that before injection (1.8 ± 0.3); the strong increment of the ratiometric signal was attributable to the accumulation of ISSzyme in the

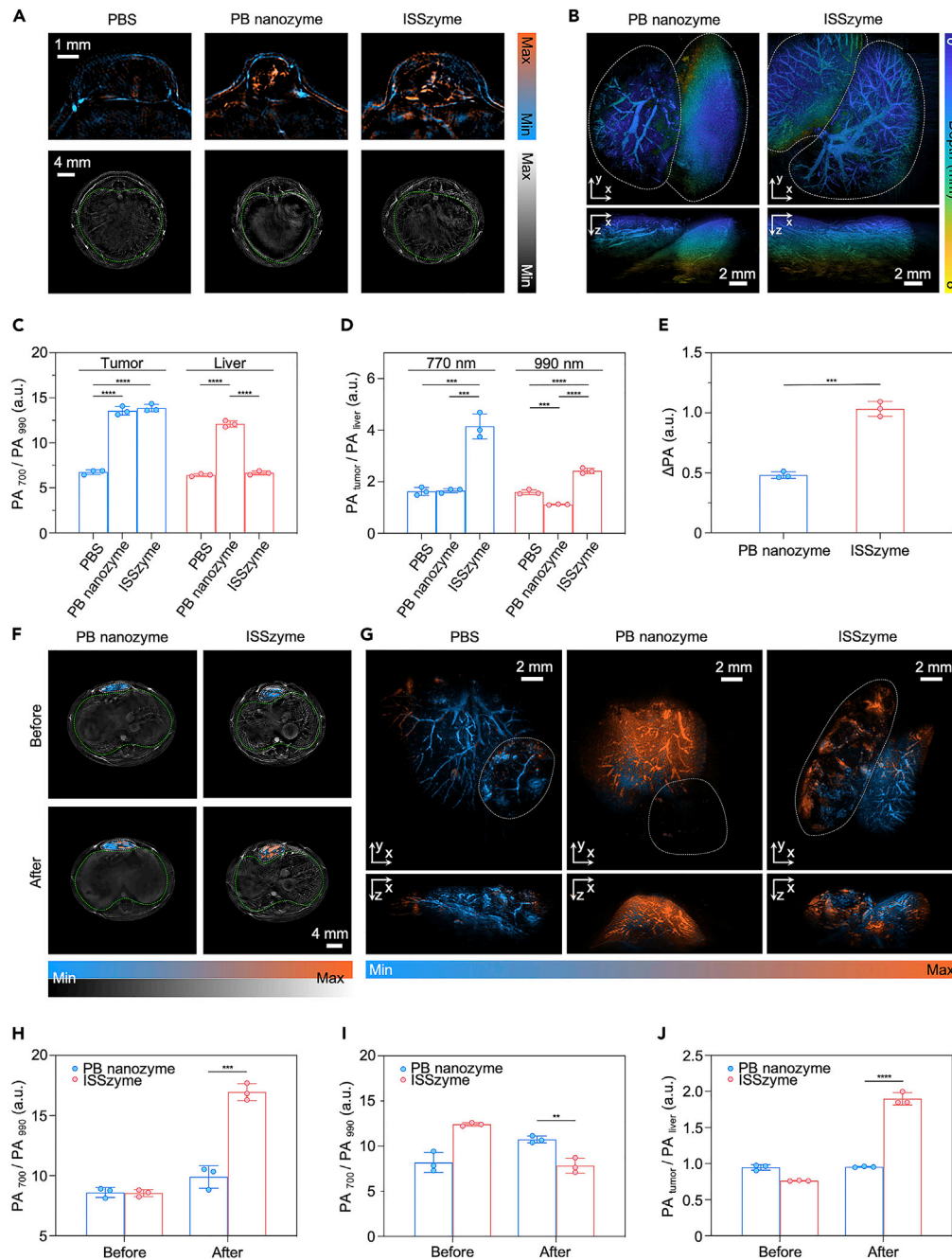


**Figure 5. Liver-accumulation-free property of ISSzyme**

(A) Representative PA images of the subcutaneous 4T1 tumor and the cross-section of the liver in mice (n = 3) at 10 h post-injection of PBS, PB nanozyme, and ISSzyme.

(B) MIP of PAMe imaging results of the right liver lobes of mice at 10 h post-injection of PBS (left column) and PB nanozyme/ISSzyme (right column).

(C) Quantification of  $PA_{700}/PA_{990}$  of the subcutaneous 4T1 tumor and the cross-section of the liver after systemic administration.

(D) Quantification of  $PA_{tumor}/PA_{liver}$  after systemic administration.

(E) Quantification of the relative PA signal of the right liver lobes of mice.

(F) Representative PA images of the cross-section of liver (green dashed) and liver metastasis of 4T1 tumor (white dashed) in mice at 10 h post-injection of PB nanozyme or ISSzyme.

**Figure 5. Continued**

(G) PAMe imaging results of the right liver lobe and liver metastasis of 4T1 tumor (dashed) at 10 h post-injection of PBS, PB nanozyme, and ISSzyme.

(H and I) Quantification of  $PA_{700}/PA_{990}$  of liver metastasis of 4T1 tumor (H) and liver (I) before and after administration.

(J) Quantification of  $PA_{tumor}/PA_{liver}$  of liver metastasis of 4T1 tumors and livers before and after administration.

tumor through the EPR effect (Figure 4D). *In vivo* fluorescence experiments achieved roughly the same results (Figure S19). All the above results demonstrated that ISSzyme can efficiently react with GSH to produce detectable PA signal changes in the tumor site, providing a viable means for tumor-specific imaging with high sensitivity and specificity.

To further study the spatial distribution of ISSzyme inside the tumors, three-dimensional *in vivo* PA images were acquired by three-dimensional PA mesoscopic (PAMe) imaging. The 4T1 xenograft tumor was implanted subcutaneously on the back of BALB/c mice. PAMe images were recorded at both 700 (Figure 4E) and 990 nm (Figure S20) before systemic administration and 10 h after the injection of ISSzyme. The reconstructed tomograms were shown as maximum intensity projection images. Compared with the tumor before systemic administration, an obvious PA signal from ISSzyme appeared in the tumor site at 700 nm. Quantitatively,  $PA_{700}/PA_{990}$  of the tumor at 10 h post-injection ( $12 \pm 1$ ) was 2.14-fold higher than that before administration ( $5.6 \pm 0.4$ ) (Figure 4F). The rate of change between 700 and 990 nm was used to distinguish ISSzyme from the background tissue, and the 3D PAMe result was pseudo-colored (Figure 4G). The localization of the ISSzyme relative to the tumor vascular network indicated the excellent targeting and specific GSH activatable capabilities of ISSzyme. The above results demonstrated that PB nanozymes were synthesized *in situ* by the application of ISSzyme, and laid the foundation for PAI-guided PTT and tumor hypoxia relief based on *in situ* synthesized nanozyme.

**Liver-accumulation-free property of ISSzyme**

Less than 0.7% (median) of the injected nanoparticles can be delivered to the solid tumor, and most nanoparticles accumulate in metabolic organs independent of the site of injection.<sup>30</sup> Therefore, the extremely low delivery efficiency of conventional nanozymes not only reduces the treatment efficiency but also leads to side effects to the metabolic organs, such as the liver and the spleen. Meanwhile, in PA molecular imaging, the strong tissue background from endogenous chromophores (mainly from oxy- and deoxy-hemoglobin) inevitably reduces imaging contrast. Therefore, it is difficult to achieve highly specific tumor imaging in organs with high levels of background from both intrinsic tissue and exogenous agents, with the liver being a representative example. The liver-accumulation-free capability of ISSzyme was validated by a series of PAI experiments. First of all, the liver accumulations of ISSzyme and PB nanozyme were measured *in vivo* using the subcutaneous 4T1 xenograft tumor models. At 10 h after systemic administration of ISSzyme or PB nanozyme, the cross-sectional PACT images of both the liver and the tumor were recorded at 700–990 nm, whereas mice treated with the same volume of PBS were imaged as a control (Figures S21 and S22). Both ISSzyme and PB nanozyme accumulated inside the tumors and the livers showed the agent-induced signal changes (Figure 5A). More quantitatively, the average values of  $PA_{700}/PA_{990}$  in the tumor with PB nanozyme ( $13.6 \pm 0.5$ ) and with ISSzyme ( $13.9 \pm 0.4$ ) were 2.03 and 2.07 times that of the control ( $6.7 \pm 0.3$ ), respectively (Figure 5C). Besides, a drastic difference could be observed in the cross-sectional images of the liver sites: compared with the control group, the liver of the group injected with PB nanozyme had lost most of the internal PA features, due to the fact that PB nanozyme accumulated in the liver to increase light attenuation. In contrast, the same level of feature richness was observed in the ISSzyme-treated group as in the control. The average value of  $PA_{700}/PA_{990}$  in the liver site with PB nanozyme ( $9.8 \pm 0.7$ ) was 1.44 and 1.36 times that of the control ( $6.8 \pm 0.2$ ) and ISSzyme ( $7.2 \pm 0.1$ ) (Figure 5C). The ratio between the average PA amplitudes in the tumor site and the liver site ( $PA_{tumor}/PA_{liver}$ ) also confirmed the above conclusion (Figure 5D). The average value of  $PA_{tumor}/PA_{liver}$  at 700 nm of the ISSzyme-treated group ( $4.15 \pm 0.49$ ) was 2.52 and 2.55 times that of the control group ( $1.65 \pm 0.08$ ) and the PB nanozyme-treated group ( $1.63 \pm 0.16$ ). This was also confirmed by Bio-TEM of *ex vivo* livers (Figure S23), where a large amount of PB nanozyme was clearly observed in the liver of the mouse injected with PB nanozyme. In contrast, no PB nanozyme was found in the liver of the mouse injected with ISSzyme. Subsequently, to further verify the liver-accumulation-free property of ISSzyme, the right liver lobes of the mice ( $n = 3$ ) at 10 h post-injection were surgically excised and fixed in agarose (Figure S24) for *ex vivo* three-dimensional PAMe imaging. Compared with the liver of the PBS-injected mice, the liver of the PB nanozyme-injected mice only exhibited strong surface signals, and the whole liver appeared bright without fine details (Figure 5B). In

contrast, the liver of the ISSzyme-injected mice showed the same level of details as the control group. Quantitatively, the relative PA signal (averaged liver signal ratio between the PB nanozyme/ISSzyme-injected mice and the PBS-injected mice,  $\Delta PA$ ) of the ISSzyme-treated group ( $1.03 \pm 0.06$ ) was 2.15-fold that of the PB nanozyme-treated group ( $0.48 \pm 0.03$ ) (Figure 5E).

To further study the performance of ISSzyme in distinguishing the tumor from healthy liver tissue, the liver metastasis of 4T1 tumor models was imaged using PACT. PA images were recorded at 700, 850, and 990 nm before systemic administration and 10 h after the injection of ISSzyme or PB nanozyme (Figure 5F). Comparing the cross-sectional PA images before and after ISSzyme treatment, the tumor could be clearly identified. The average value of  $PA_{700}/PA_{990}$  in the tumor of the ISSzyme-treated mice ( $16.9 \pm 0.7$ ) increased 1.97 times compared to the value before treatment ( $8.6 \pm 0.6$ ), indicating ISSzyme accumulation and PB nanozyme formation (Figure 5H). In contrast, the value of  $PA_{700}/PA_{990}$  of the PB nanozyme-treated mice ( $9.9 \pm 0.9$ ) was almost unchanged compared to that before treatment ( $8.6 \pm 0.4$ ). The value of  $PA_{700}/PA_{990}$  of the liver site was almost unchanged (Figure 5I). This could be caused by the decrease in light intensity in the tumor due to the accumulation of PB nanozyme in the whole liver. Concretely, the value of  $PA_{\text{tumor}}/PA_{\text{liver}}$  stayed constant for the group treated with PB nanozyme, whereas  $PA_{\text{tumor}}/PA_{\text{liver}}$  of the mice treated with ISSzyme ( $1.9 \pm 0.1$ ) was 2.71-fold higher than that before injection ( $0.7 \pm 0.1$ ), making the tumor more distinguishable from the liver background (Figure 5J).

To further confirm the results, the right liver lobes with the metastatic tumor were isolated at 10 h post-injection and fixed with agarose (Figure S25) for *ex vivo* PAME imaging (Figure 5G). For the PBS-treated group, blood vessels in the right liver lobes and the tumor were clearly visible. However, there was a large amount of PB nanozyme accumulated in the right liver lobes of the PB nanozyme-treated group. Furthermore, the signal from the tumor was overwhelmed by the strong signal from the liver. In sharp contrast, for the ISSzyme-treated group, signals from both the liver and the tumor were observable. Overall, the above results demonstrated the liver-accumulation-free performance of ISSzyme and suggested that ISSzyme-mediated PAI was capable of *in situ* differentiation of metastatic tumor and the liver background.

### In vivo therapeutics and tumor hypoxia relief

Before *in vivo* therapeutics, the photothermal capability of ISSzyme was demonstrated *in vivo*. Mice were treated with ISSzyme ( $13 \text{ mg kg}^{-1}$ ) or the same volume of PBS. At 10 h post-injection, all mice were irradiated by a NIR laser (808 nm,  $2 \text{ W cm}^{-2}$ ) for 10 min. Meanwhile, an IR radiation thermal camera was used to record the real-time temperatures at 30-s intervals (Figure S26). The tumor temperature of the ISSzyme-treated mice gradually increased and achieved a maximum of  $62.0^\circ\text{C}$ , while the tumor temperature of the PBS-treated mice did not increase (Figure S27). These results demonstrated that during the ISSzyme treatment, PB nanozyme can be synthesized *in situ* for highly efficient PTT. The *in vivo* therapeutic performance of ISSzyme was investigated in 4T1 tumor-bearing BALB/c mice. The mice were randomly divided into 4 groups ( $n = 5$ ), labeled "control", "laser", "ISSzyme", and "ISSzyme + laser". Each group received repeated systemic administrations of ISSzyme ( $13 \text{ mg kg}^{-1}$ ) or the same volume of PBS on days 0, 2, 4, and 6. For the "laser" and the "ISSzyme + laser" groups, the tumor sites of the mice were irradiated with a NIR laser (808 nm,  $2 \text{ W cm}^{-2}$ ) for 10 min at 10 h after the first systemic administration. The tumor volumes were monitored every two days to evaluate the therapeutic effect (Figure 6A). The growth of the tumors receiving both ISSzyme and laser irradiation was significantly suppressed, indicating the substantial therapeutic efficacy of PTT. In contrast, the tumor growth of other groups treated with PBS, laser, or ISSzyme alone showed negligible inhibition effect. Moreover, the body weights (Figure 6B) of the mice were recorded during the therapeutic procedures, indicating no obvious biotoxicity during the therapeutic process. In addition, the morphology and weight of the resected tumors confirmed the above conclusions (Figures S28 and S29). Pathological analyses, including hematoxylin and eosin (H&E), terminal deoxynucleotidyl transferase-mediated deoxyuridine triphosphate nick end labeling (TUNEL), and Ki-67 staining, were used to study the pathological variation and mechanism of ISSzyme-induced PTT (Figure 6D). For the two laser-treated groups, tumors were resected  $\sim 5$  h after laser irradiation, while for the other groups tumors were collected  $\sim 15$  h after the last systemic administration. According to the H&E staining results, the "ISSzyme + laser" group showed a decrease in the number of cell nuclei, and obvious cell shrinkage and injury, while ISSzyme treatment or laser treatment alone exhibited negligible effect. For the TUNEL staining, strong green fluorescence was only found in the "ISSzyme + laser" group, indicating the presence of apoptotic tumor cells. On the contrary, the "ISSzyme + laser" group exhibited the weakest fluorescence

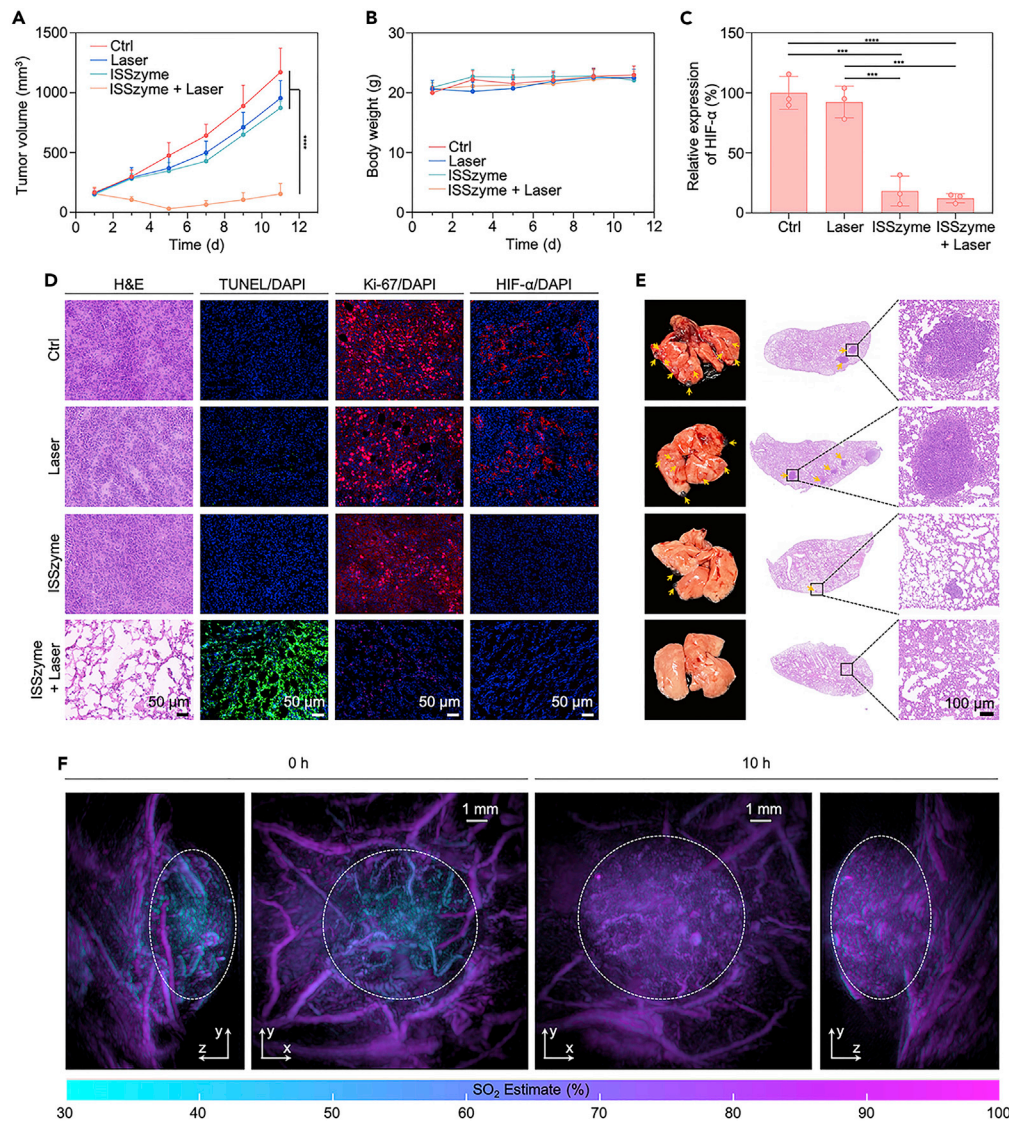


**Figure 6. In vivo therapeutics and tumor hypoxia relief**

(A and B) Tumor growth curves (A) and body weights (B) of different groups after different treatments. (C) Relative expression of HIF- $\alpha$  after different treatment. (D) Histopathological analysis of the excised tumor slices after different treatments, including H&E staining, TUNEL assay, Ki-67 staining, and HIF- $\alpha$  staining. (E) Picture of metastasis in lungs and H&E-stained lung section in the groups with different treatments. (F) 3D PAMe images of SO<sub>2</sub> taken at 0 and 10 h after ISSzyme treatment.

in the Ki-67 staining results, indicating that the proliferation of tumor cells was seriously impaired by the ISSzyme-induced PTT.

The tumor hypoxia relief efficiency of ISSzyme was examined in 4T1-bearing BALB/c mice by measuring the HIF- $\alpha$  expression. The red fluorescence intensity of HIF-1 $\alpha$  in the two ISSzyme-treated groups was weak, while the control group and the “laser” group showed strong fluorescence, suggesting the hypoxia relieving ability of ISSzyme (Figure 6D). Quantitatively, the HIF-1 $\alpha$  expression in the “ISSzyme + laser” group was only ~12.17% that of the control group (Figure 6C), confirming that the *in situ* synthesized PB nanozyme through the ISSzyme treatment can effectively decompose H<sub>2</sub>O<sub>2</sub>, and the generated O<sub>2</sub> can relieve tumor hypoxia. Moreover, lung metastasis of the 4T1 tumor was investigated after 11 days post-treatment to study the metastasis inhibition efficiency (Figure 6E). Metastasis tumors were observed almost everywhere

in the lungs of the control group and the “laser” group, while the two ISSzyme-treated groups showed little or no sign of metastasis in the lungs. In addition, H&E staining was used to investigate the metastatic lesions, which were shown as cell clusters with dark stained nuclei. The metastatic foci could be evidently detected in the control group and the laser group, but were barely visualized in the two ISSzyme-treated groups. In addition, the blood oxygen saturation (SO<sub>2</sub>) in the tumor before and after ISSzyme treatment was monitored by multispectral 3D PAME *in vivo*. The results showed that *in situ* synthesized PB nanozyme effectively alleviated hypoxia (Figure 6F). Therefore, ISSzyme can significantly inhibit lung metastasis of breast cancer, due to the hypoxia relief effect through the PB nanozyme synthesized *in situ*.

## DISCUSSION

Artificial nanozymes have attracted extensive research interest in the past decade. They exhibit adjustable catalytic activity, a variety of enzyme-like activities and high stability, allowing for applications in various fields such as biosensing, disease monitoring, and disease treatment. However, before exploiting its full potential in biomedical applications, nanozymes are still facing questions such as biocompatibility, biodegradability, and biotoxicity. In addition, the extremely low delivery efficiency of the nanoparticles necessitates increased dosage. In this study, we have shown that these obstacles can be overcome through a strategy of synthesizing nanozymes *in situ*.

By comparing ISSzyme with the conventional PB nanozyme, we confirmed the feasibility of *in situ* synthesis of nanozyme. ISSzyme not only has the effect of tumor theranostics and hypoxia relief as traditional PB nanozymes do but also enjoys the unprecedented advantage of minimal accumulation in metabolic organs such as the liver. In addition, ISSzyme can respond to GSH in the TME to enable PAI-guided PTT while simultaneously reducing damage to normal tissues during the treatment.

In conclusion, ISSzyme is a newly developed nanomedicine for cancer treatment and tumor hypoxia relief. ISSzyme can synthesize PB nanozyme *in situ* when reacting with GSH, a highly expressed substance in tumors. The intratumorally generated PB nanozyme has catalase-like activity, which can decompose H<sub>2</sub>O<sub>2</sub> to produce O<sub>2</sub>, so as to relieve tumor hypoxia and inhibit metastasis. The strong NIR absorption of PB nanozyme makes ISSzyme a potential candidate for PA-guided PTT. Moreover, the high sensitivity and specificity of ISSzyme to GSH was instrumental in reducing false-positive image signals and treatment side effects. The demonstrated “liver-accumulation-free” property not only reduces damage to the liver and other metabolic organs but also helps tumor identification from a strong intrinsic background. In addition, the ISSzyme has shown high biocompatibility in both *in vitro* and *in vivo* assessments. Given the above advantages of ISSzyme, the first-of-its-kind strategy of synthesizing nanozymes *in situ* is expected to shed light on the design and application of future artificial enzymes.

## Limitations of the study

We have presented a new strategy of synthesizing nanozymes *in situ* for cancer treatment and tumor hypoxia relief. Although the *in situ* synthesized PB nanozyme has catalase-like activity and is capable of tumor-specific and liver-accumulation-free PAI and PTT, more catalytic properties of nanozyme should be studied.

## STAR★METHODS

Detailed methods are provided in the online version of this paper and include the following:

- KEY RESOURCES TABLE
- RESOURCE AVAILABILITY
  - Lead contact
  - Materials availability
  - Data and code availability
- EXPERIMENTAL MODEL AND SUBJECT DETAILS
  - Animals and tumor models
- METHOD DETAILS
  - Synthesis of ISSzyme
  - Characterization of ISSzyme
  - GSH-responsiveness of ISSzyme
  - PA spectroscopic measurement

- Photothermal properties
- *In vitro* O<sub>2</sub> generation
- *In vitro* biocompatibility of ISSzyme
- *In vitro* cytotoxicity assay of ISSzyme
- *In vitro* O<sub>2</sub> generation at the cellular level
- *In vitro* invasion assay
- *In vitro* apoptosis evaluation
- *In vivo* biocompatibility of ISSzyme
- *In vivo* biodistribution of ISSzyme
- *In vivo* PACT imaging
- *In vivo* and *ex vivo* PAMe imaging
- *In vivo* thermal imaging
- *In vivo* therapeutic performance of ISSzyme
- Pathological investigation
- *In vivo* metastasis inhibition of ISSzyme
- *In vivo* SO<sub>2</sub> monitoring
- Data processing and image reconstruction
- **QUANTIFICATION AND STATISTICAL ANALYSIS**

## SUPPLEMENTAL INFORMATION

Supplemental information can be found online at <https://doi.org/10.1016/j.isci.2023.106066>.

## ACKNOWLEDGMENTS

The work was financially supported by the National Natural Science Foundation of China (32271443, 61971265, 61735016), the Innovation Fund of Fuzhou Institute for Data Technology, grants from Tsinghua University Institute for Precision Healthcare, and Tsinghua-Foshan Institute of Advanced Manufacturing, the Beijing Natural Science Foundation (JQ22024), and grants from Peking University Third Hospital (BY-SYZD2019018, jyzc2018-02, and BYSY2015023).

## AUTHOR CONTRIBUTIONS

C.M. and X.L. designed the research; C.C., Y.C., L.Z., and X.W. performed the research; All authors analyzed and interpreted the data; C.M., X.L., and C.C. wrote the paper.

## DECLARATION OF INTERESTS

C.M. has a financial interest in TsingPAI Technology Co., Ltd., which did not support this work. C.M., X.L., C.C., and L.Z. have applied for patents (Chinese Patent Application No.: ZL202111317626.1) related to the work reported in this manuscript.

Received: August 24, 2022

Revised: November 27, 2022

Accepted: January 23, 2023

Published: January 26, 2023

## REFERENCES

1. Ai, Y., Hu, Z., Liang, X., Sun, H., Xin, H., and Liang, Q. (2021). Recent advances in nanozymes: from matters to bioapplications. *Adv. Funct. Mater.* **32**, 2110432. <https://doi.org/10.1002/adfm.202110432>.
2. Robert, A., and Meunier, B. (2022). How to define a nanozyme. *ACS Nano* **16**, 6956–6959. <https://doi.org/10.1021/acsnano.2c02966>.
3. Zhang, X., Li, G., Chen, G., Wu, D., Wu, Y., and James, T.-D. (2021). Enzyme mimics for engineered biomimetic cascade nanoreactors: mechanism, applications, and prospects. *Adv. Funct. Mater.* **31**, 2106139. <https://doi.org/10.1002/adfm.202106139>.
4. Wang, H., Wan, K., and Shi, X. (2019). Recent advances in nanozyme research. *Adv. Mater.* **31**, e1805368. <https://doi.org/10.1002/adma.201805368>.
5. Huang, Y., Ren, J., and Qu, X. (2019). Nanozymes: classification, catalytic mechanisms, activity regulation, and applications. *Chem. Rev.* **119**, 4357–4412. <https://doi.org/10.1021/acs.chemrev.8b00672>.
6. Ma, Z., Foda, M.-F., Liang, H., Zhao, Y., and Han, H. (2021). In situ nanozyme-amplified NIR-II phototheranostics for tumor-specific imaging and therapy. *Adv. Funct. Mater.* **31**, 2103765. <https://doi.org/10.1002/adfm.202103765>.
7. Hu, Y., Cheng, H., Zhao, X., Wu, J., Muhammad, F., Lin, S., He, J., Zhou, L., Zhang, C., Deng, Y., et al. (2017). Surface-enhanced Raman scattering active gold nanoparticles with enzyme-mimicking activities for measuring glucose and lactate in living tissues. *ACS Nano* **11**, 5558–5566. <https://doi.org/10.1021/acsnano.7b00905>.

8. Sharma, T.K., Ramanathan, R., Weerathunge, P., Mohammadtaheri, M., Daima, H.-K., Shukla, R., and Bansal, V. (2014). Aptamer-mediated 'turn-off/turn-on' nanozyme activity of gold nanoparticles for kanamycin detection. *Chem. Commun.* 50, 15856–15859. <https://doi.org/10.1039/c4cc07275h>.
9. Wang, Z., Zhang, Y., Ju, E., Liu, Z., Cao, F., Chen, Z., Ren, J., and Qu, X. (2018). Biomimetic nanoflowers by self-assembly of nanozymes to induce intracellular oxidative damage against hypoxic tumors. *Nat. Commun.* 9, 3334. <https://doi.org/10.1038/s41467-018-05798-x>.
10. Zhang, Y., Wang, X., Chu, C., Zhou, Z., Chen, B., Pang, X., Lin, G., Lin, H., Guo, Y., Ren, E., et al. (2020). Genetically engineered magnetic nanocages for cancer magneto-catalytic theranostics. *Nat. Commun.* 11, 5421. <https://doi.org/10.1038/s41467-020-19061-9>.
11. Wang, D., Wu, H., Wang, C., Gu, L., Chen, H., Jana, D., Feng, L., Liu, J., Wang, X., Xu, P., et al. (2021). Self-assembled single-site nanozyme for tumor-specific amplified cascade enzymatic therapy. *Angew. Chem. Int. Ed. Engl.* 60, 3001–3007. <https://doi.org/10.1002/anie.202008868>.
12. Yue, S., Zhang, P., Qin, M., Zhu, L., Qiao, Y., Li, Q., Lu, Y., Wu, H., Jiang, N., Liu, C., et al. (2022). An enzyme-like activity nanoprobe based on Fe(III)-rutin hydrate biomineral for MR imaging and therapy of triple negative breast cancer. *Adv. Funct. Mater.* 32, 2202848. <https://doi.org/10.1002/adfm.202202848>.
13. Wang, Z., Liu, B., Sun, Q., Feng, L., He, F., Yang, P., Gai, S., Quan, Z., and Lin, J. (2021). Upconverted metal-organic framework Janus architecture for near-infrared and ultrasound Co-enhanced gigh performance tumor therapy. *ACS Nano* 15, 12342–12357. <https://doi.org/10.1021/acsnano.1c04280>.
14. Yang, L., Zhu, H., Zhao, R., Zhang, Z., Liu, B., Gong, H., Zhu, Y., Ding, H., Gai, S., and Feng, L. (2022). Tumor microenvironment activated glutathione self-depletion theranostic nanocapsules for imaging-directed synergistic cancer therapy. *Chem. Eng. J.* 450, 138137. <https://doi.org/10.1016/j.cej.2022.138137>.
15. Feng, L., Liu, B., Xie, R., Wang, D., Qian, C., Zhou, W., Liu, J., Jana, D., Yang, P., and Zhao, Y. (2020). An ultrasmlant SnFe<sub>2</sub>O<sub>4</sub> nanozyme with endogenous oxygen generation and glutathione depletion for synergistic cancer therapy. *Adv. Funct. Mater.* 31, 2006216. <https://doi.org/10.1002/adfm.202006216>.
16. Gao, F., Shao, T., Yu, Y., Xiong, Y., and Yang, L. (2021). Surface-bound reactive oxygen species generating nanozymes for selective antibacterial action. *Nat. Commun.* 12, 745. <https://doi.org/10.1038/s41467-021-20965-3>.
17. Chen, Z., Wang, Z., Ren, J., and Qu, X. (2018). Enzyme mimicry for combating bacteria and biofilms. *Acc. Chem. Res.* 51, 789–799. <https://doi.org/10.1021/acs.accounts.8b00011>.
18. Vernekar, A.-A., Sinha, D., Srivastava, S., Paramasivam, P.-U., D'Silva, P., and Mugesh, G. (2014). An antioxidant nanozyme that uncovers the cytoprotective potential of vanadia nanowires. *Nat. Commun.* 5, 5301. <https://doi.org/10.1038/ncomms6301>.
19. Cao, F., Zhang, L., You, Y., Zheng, L., Ren, J., and Qu, X. (2020). An enzyme-mimicking single-atom catalyst as an efficient multiple reactive oxygen and nitrogen species scavenger for sepsis management. *Angew. Chem. Int. Ed. Engl.* 59, 5108–5115. <https://doi.org/10.1002/anie.201912182>.
20. Huang, Y., Liu, Z., Liu, C., Ju, E., Zhang, Y., Ren, J., and Qu, X. (2016). Self-assembly of multi-nanozymes to mimic an intracellular antioxidant defense system. *Angew. Chem. Int. Ed. Engl.* 55, 6646–6650. <https://doi.org/10.1002/anie.201600868>.
21. Xi, J., Zhang, R., Wang, L., Xu, W., Liang, Q., Li, J., Jiang, J., Yang, Y., Yan, X., Fan, K., and Gao, L. (2020). A nanozyme-based artificial peroxisome ameliorates hyperuricemia and ischemic stroke. *Adv. Funct. Mater.* 31, 2007130. <https://doi.org/10.1002/adfm.202007130>.
22. Ma, X., Hao, J., Wu, J., Li, Y., Cai, X., and Zheng, Y. (2022). Prussian blue nanozyme as a pyroptosis inhibitor alleviates neurodegeneration. *Adv. Mater.* 34, e2106723. <https://doi.org/10.1002/adma.202106723>.
23. Chen, J., Ma, Q., Li, M., Chao, D., Huang, L., Wu, W., Fang, Y., and Dong, S. (2021). Glucose-oxidase like catalytic mechanism of noble metal nanozymes. *Nat. Commun.* 12, 3375. <https://doi.org/10.1038/s41467-021-23737-1>.
24. Liu, B., Sun, Z., Huang, P.J.J., and Liu, J. (2015). Hydrogen peroxide displacing DNA from nanoceria: mechanism and detection of glucose in serum. *J. Am. Chem. Soc.* 137, 1290–1295. <https://doi.org/10.1021/ja511444e>.
25. Ly, H.G.T., Absillis, G., Janssens, R., Proost, P., and Parac-Vogt, T.-N. (2015). Highly amino acid selective hydrolysis of myoglobin at aspartate residues as promoted by zirconium(IV)-substituted polyoxometalates. *Angew. Chem. Int. Ed. Engl.* 54, 7391–7394. <https://doi.org/10.1002/anie.201502006>.
26. Zhang, J., Wu, S., Ma, L., Wu, P., and Liu, J. (2020). Graphene oxide as a photocatalytic nuclease mimicking nanozyme for DNA cleavage. *Nano Res.* 13, 455–460. <https://doi.org/10.1007/s12274-020-2629-8>.
27. Tao, Y., Ju, E., Ren, J., and Qu, X. (2014). Polypyrrole nanoparticles as promising enzyme mimics for sensitive hydrogen peroxide detection. *Chem. Commun.* 50, 3030–3032. <https://doi.org/10.1039/c4cc00328d>.
28. Fan, K., Xi, J., Fan, L., Wang, P., Zhu, C., Tang, Y., Xu, X., Liang, M., Jiang, B., Yan, X., and Gao, L. (2018). In vivo guiding nitrogen-doped carbon nanozyme for tumor catalytic therapy. *Nat. Commun.* 9, 1440. <https://doi.org/10.1038/s41467-018-03903-8>.
29. Zhang, L., Zhang, L., Deng, H., Li, H., Tang, W., Guan, L., Qiu, Y., Donovan, M.J., Chen, Z., and Tan, W. (2021). In vivo activation of pH-responsive oxidase-like graphitic nanozymes for selective killing of *Helicobacter pylori*. *Nat. Commun.* 12, 2002. <https://doi.org/10.1038/s41467-021-22286-x>.
30. Wilhelm, S., Tavares, A.-J., Dai, Q., Ohta, S., Audet, J., Dvorak, H.-F., and Chan, W.C.W. (2016). Analysis of nanoparticle delivery to tumours. *Nat. Rev. Mater.* 1, 16014. <https://doi.org/10.1038/natrevmats.2016.14>.
31. Mitchell, M.-J., Billingsley, M.-M., Haley, R.-M., Wechsler, M.-E., Peppas, N.-A., and Langer, R. (2021). Engineering precision nanoparticles for drug delivery. *Nat. Rev. Drug Discov.* 20, 101–124. <https://doi.org/10.1038/s41573-020-0090-8>.
32. Wang, H., Thorling, C.-A., Liang, X., Bridle, K.-R., Grice, J.-E., Zhu, Y., Crawford, D.H.G., Xu, Z.-P., Liu, X., and Roberts, M.-S. (2015). Diagnostic imaging and therapeutic application of nanoparticles targeting the liver. *J. Mater. Chem. B* 3, 939–958. <https://doi.org/10.1039/c4tb01611d>.
33. Cesaratto, L., Vascotto, C., Calligaris, S., and Tell, G. (2004). The importance of redox state in liver damage. *Ann. Hepatol.* 3, 86–92. [https://doi.org/10.1016/s1665-2681\(19\)32099-x](https://doi.org/10.1016/s1665-2681(19)32099-x).
34. Zhang, W., Wang, J., Xie, Z., Zou, H., Chen, Q., Xu, L., Hu, L., Fang, N., Xu, J., Zhou, J., et al. (2022). Antithrombotic therapy by regulating the ROS-mediated thrombosis microenvironment and specific nonpharmaceutical thrombolysis using Prussian blue nanodroplets. *Small* 18, e2106252. <https://doi.org/10.1002/sml.202106252>.
35. Qin, Z., Li, Y., and Gu, N. (2018). Progress in applications of Prussian blue nanoparticles in biomedicine. *Adv. Healthc. Mater.* 7, e1800347. <https://doi.org/10.1002/adhm.201800347>.
36. Lu, D., Jiang, H., Zhang, G., Luo, Q., Zhao, Q., and Shi, X. (2021). An in situ generated Prussian blue nanoparticle-mediated multimode nanozyme-linked immunosorbent assay for the detection of aflatoxin B1. *ACS Appl. Mater. Interfaces* 13, 25738–25747. <https://doi.org/10.1021/acsmi.1c04751>.
37. Bai, H., Kong, F., Feng, K., Zhang, X., Dong, H., Liu, D., Ma, M., Liu, F., Gu, N., and Zhang, Y. (2021). Prussian blue nanozymes prevent anthracycline-induced liver injury by attenuating oxidative stress and regulating inflammation. *ACS Appl. Mater. Interfaces* 13, 42382–42395. <https://doi.org/10.1021/acsmi.1c09838>.
38. Li, Z.-H., Chen, Y., Sun, Y., and Zhang, X.-Z. (2021). Platinum-doped Prussian blue nanozymes for multiwavelength bioimaging guided photothermal therapy of tumor and anti-inflammation. *ACS Nano* 15, 5189–5200. <https://doi.org/10.1021/acsnano.0c10388>.
39. Gao, Y., Yu, G., Xing, K., Gorin, D., Kotelevtsev, Y., Tong, W., and Mao, Z. (2020). Finely tuned Prussian blue-based nanoparticles and their application in disease

- treatment. *J. Mater. Chem. B* 8, 7121–7134. <https://doi.org/10.1039/d0tb01248c>.
40. Gao, X., Wang, Q., Cheng, C., Lin, S., Lin, T., Liu, C., and Han, X. (2020). The application of Prussian blue nanoparticles in tumor diagnosis and treatment. *Sensors* 20, 6905. <https://doi.org/10.3390/s20236905>.
41. Huang, Y., Xu, Q., Zhang, J., Yin, Y., Pan, Y., Zheng, Y., Cai, X., Xia, Q., and He, K. (2022). Prussian blue scavenger ameliorates hepatic ischemia-reperfusion injury by inhibiting inflammation and reducing oxidative stress. *Front. Immunol.* 13, 891351. <https://doi.org/10.3389/fimmu.2022.891351>.
42. Xie, X., Gao, W., Hao, J., Wu, J., Cai, X., and Zheng, Y. (2021). Self-synergistic effect of Prussian blue nanoparticles for cancer therapy: driving photothermal therapy and reducing hyperthermia-induced side effects. *J. Nanobiotechnology* 19, 126. <https://doi.org/10.1186/s12951-021-00819-2>.
43. Fitzgerald, R.-C., Antoniou, A.-C., Fruk, L., and Rosenfeld, N. (2022). The future of early cancer detection. *Nat. Med.* 28, 666–677. <https://doi.org/10.1038/s41591-022-01746-x>.
44. Mallidi, S., Luke, G.-P., and Emelianov, S. (2011). Photoacoustic imaging in cancer detection, diagnosis, and treatment guidance. *Trends Biotechnol.* 29, 213–221. <https://doi.org/10.1016/j.tibtech.2011.01.006>.
45. Wang, L.-V., and Hu, S. (2012). Photoacoustic tomography: in vivo imaging from organelles to organs. *Science* 335, 1458–1462. <https://doi.org/10.1126/science.1216210>.
46. Ntziachristos, V., and Razansky, D. (2010). Molecular imaging by means of multispectral optoacoustic tomography (MSOT). *Chem. Rev.* 110, 2783–2794. <https://doi.org/10.1021/cr9002566>.
47. Razansky, D., Distel, M., Vinegoni, C., Ma, R., Perrimon, N., Köster, R.W., and Ntziachristos, V. (2009). Multispectral opto-acoustic tomography of deep-seated fluorescent proteins in vivo. *Nat. Photonics* 3, 412–417. <https://doi.org/10.1038/nphoton.2009.98>.
48. Jathoul, A.-P., Laufer, J., Ogunlade, O., Treeby, B., Cox, B., Zhang, E., Johnson, P., Pizzey, A.-R., Philip, B., Marafioti, T., et al. (2015). Deep in vivo photoacoustic imaging of mammalian tissues using a tyrosinase-based genetic reporter. *Nat. Photonics* 9, 239–246. <https://doi.org/10.1038/nphoton.2015.22>.
49. Zhang, H.-F., Maslov, K., Sivaramakrishnan, M., Stoica, G., and Wang, L.-V. (2007). Imaging of hemoglobin oxygen saturation variations in single vessels in vivo using photoacoustic microscopy. *Appl. Phys. Lett.* 90, 053901. <https://doi.org/10.1063/1.2435697>.
50. Wang, X., Xie, X., Ku, G., Wang, L.-V., and Stoica, G. (2006). Noninvasive imaging of hemoglobin concentration and oxygenation in the rat brain using high-resolution photoacoustic tomography. *J. Biomed. Opt.* 11, 024015. <https://doi.org/10.1117/1.2192804>.
51. Allen, T.-J., Hall, A., Dhillon, A.-P., Owen, J.-S., and Beard, P.-C. (2012). Spectroscopic photoacoustic imaging of lipid-rich plaques in the human aorta in the 740 to 1400 nm wavelength range. *J. Biomed. Opt.* 17, 061209. <https://doi.org/10.1117/1.Jbo.17.6.061209>.
52. Chen, R., Huang, S., Lin, T., Ma, H., Shan, W., Duan, F., Lv, J., Zhang, J., Ren, L., and Nie, L. (2021). Photoacoustic molecular imaging-escorted adipose photodynamic-browning synergy for fighting obesity with virus-like complexes. *Nat. Nanotechnol.* 16, 455–465. <https://doi.org/10.1038/s41565-020-00844-6>.
53. Zhang, X., Zhang, H.-F., Puliafito, C.-A., and Jiao, S. (2011). Simultaneous in vivo imaging of melanin and lipofuscin in the retina with photoacoustic ophthalmoscopy and autofluorescence imaging. *J. Biomed. Opt.* 16, 080504. <https://doi.org/10.1117/1.3606569>.
54. Zhang, Y., Cai, X., Wang, Y., Zhang, C., Li, L., Choi, S.W., Wang, L.-V., and Xia, Y. (2011). Noninvasive photoacoustic microscopy of living cells in two and three dimensions through enhancement by a metabolite dye. *Angew. Chem. Int. Ed. Engl.* 50, 7359–7363. <https://doi.org/10.1002/anie.201101659>.
55. Zhang, Y., Jeon, M., Rich, L.-J., Hong, H., Geng, J., Zhang, Y., Shi, S., Barnhart, T.-E., Alexandridis, P., Huiying, J.-D., et al. (2014). Non-invasive multimodal functional imaging of the intestine with frozen micellar naphthalocyanines. *Nat. Nanotechnol.* 9, 631–638. <https://doi.org/10.1038/nnano.2014.130>.
56. Mokrousov, M.-D., Thompson, W., Ermilov, S.-A., Abakumova, T., Novoselova, M.-V., Inozemtseva, O.-A., Zatsepina, T.-S., Zharov, V.-P., Galanzha, E.-I., and Gorin, D.-A. (2021). Indocyanine green dye based bimodal contrast agent tested by photoacoustic/fluorescence tomography setup. *Biomed. Opt. Express* 12, 3181–3195. <https://doi.org/10.1364/BOE.419461>.
57. Mokrousov, M.-D., Novoselova, M.-V., Nolan, J., Harrington, W., Rudakovskaya, P., Bratashov, D.-N., Galanzha, E.-I., Fuenzalida-Werner, J.-P., Yakimov, B.-P., Nazarikov, G., et al. (2019). Amplification of photoacoustic effect in bimodal polymer particles by self-quenching of indocyanine green. *Biomed. Opt. Express* 10, 4775–4789. <https://doi.org/10.1364/BOE.10.004775>.
58. Novoselova, M.-V., German, S.-V., Abakumova, T.-O., Perevoschikov, S.-V., Sergeeva, O.-V., Nesterchuk, M.-V., Efimova, O.-I., Petrov, K.-S., Chernyshev, V.-S., Zatsepina, T.-S., and Gorin, D.-A. (2021). Multifunctional nanostructured drug delivery carriers for cancer therapy: multimodal imaging and ultrasound-induced drug release. *Colloids Surf. B Biointerfaces* 200, 111576. <https://doi.org/10.1016/j.colsurfb.2021.111576>.
59. Nie, L., Huang, P., Li, W., Yan, X., Jin, A., Wang, Z., Tang, Y., Wang, S., Zhang, X., Niu, G., and Chen, X. (2014). Early-stage imaging of nanocarrier-enhanced chemotherapy response in living subjects by scalable photoacoustic microscopy. *ACS Nano* 8, 12141–12150. <https://doi.org/10.1021/nl505989e>.
60. Kim, J.-W., Galanzha, E.-I., Shashkov, E.-V., Moon, H.-M., and Zharov, V.-P. (2009). Golden carbon nanotubes as multimodal photoacoustic and photothermal high-contrast molecular agents. *Nat. Nanotechnol.* 4, 688–694. <https://doi.org/10.1038/nnano.2009.231>.
61. Pu, K., Mei, J., Jokerst, J.-V., Hong, G., Antaris, A.-L., Chattopadhyay, N., Shuhendler, A.-J., Kurosawa, T., Zhou, Y., Gambhir, S.-S., et al. (2015). Diketopyrrolopyrrole-based semiconducting polymer nanoparticles for in vivo photoacoustic imaging. *Adv. Mater.* 27, 5184–5190. <https://doi.org/10.1002/adma.201502285>.
62. Pu, K., Shuhendler, A.-J., Jokerst, J.-V., Mei, J., Gambhir, S.-S., Bao, Z., and Rao, J. (2014). Semiconducting polymer nanoparticles as photoacoustic molecular imaging probes in living mice. *Nat. Nanotechnol.* 9, 233–239. <https://doi.org/10.1038/nnano.2013.302>.
63. Gong, F., Cheng, L., Yang, N., Jin, Q., Tian, L., Wang, M., Li, Y., and Liu, Z. (2018). Bimetallic oxide MnMoO<sub>x</sub> nanorods for in vivo photoacoustic imaging of GSH and tumor-specific photothermal therapy. *Nano Lett.* 18, 6037–6044. <https://doi.org/10.1021/acs.nanolett.8b02933>.
64. Wang, P., Yang, W., Shen, S., Wu, C., Wen, L., Cheng, Q., Zhang, B., and Wang, X. (2019). Differential diagnosis and precision therapy of two typical malignant cutaneous tumors leveraging their tumor microenvironment: a photomedicine strategy. *ACS Nano* 13, 11168–11180. <https://doi.org/10.1021/acsnano.9b04070>.
65. Lei, S., Zhang, J., Blum, N.-T., Li, M., Zhang, D.-Y., Yin, W., Zhao, F., Lin, J., and Huang, P. (2022). In vivo three-dimensional multispectral photoacoustic imaging of dual enzyme-driven cyclic cascade reaction for tumor catalytic therapy. *Nat. Commun.* 13, 1298. <https://doi.org/10.1038/s41467-022-29082-1>.
66. Ding, H., Cai, Y., Gao, L., Liang, M., Miao, B., Wu, H., Liu, Y., Xie, N., Tang, A., Fan, K., et al. (2019). Exosome-like nanozyme vesicles for H<sub>2</sub>O<sub>2</sub>-responsive catalytic photoacoustic imaging of xenograft nasopharyngeal carcinoma. *Nano Lett.* 19, 203–209. <https://doi.org/10.1021/acs.nanolett.8b03709>.
67. Li, L., Shemetov, A.-A., Balaban, M., Hu, P., Zhu, L., Shcherbakova, D.-M., Zhang, R., Shi, J., Yao, J., Wang, L.-V., and Verkhusha, V.-V. (2018). Small near-infrared photochromic protein for photoacoustic multi-contrast imaging and detection of protein interactions in vivo. *Nat. Commun.* 9, 2734. <https://doi.org/10.1038/s41467-018-05231-3>.
68. Xiao, H., Wu, C., Li, P., Gao, W., Zhang, W., Zhang, W., Tong, L., and Tang, B. (2017). Ratiometric photoacoustic imaging of endoplasmic reticulum polarity in injured liver tissues of diabetic mice. *Chem. Sci.* 8, 7025–7030. <https://doi.org/10.1039/c7sc02330h>.

69. Wang, Z., Zhen, X., Upputuri, P.-K., Jiang, Y., Lau, J., Pramanik, M., Pu, K., and King, B. (2019). Redox-activatable and acid-enhanced nanotheranostics for second near-infrared photoacoustic tomography and combined photothermal tumor therapy. *ACS Nano* **13**, 5816–5825. <https://doi.org/10.1021/acsnano.9b01411>.
70. Lucero, M.-Y., and Chan, J. (2021). Photoacoustic imaging of elevated glutathione in models of lung cancer for companion diagnostic applications. *Nat. Chem.* **13**, 1248–1256. <https://doi.org/10.1038/s41557-021-00804-0>.
71. Yin, C., Tang, Y., Li, X., Yang, Z., Li, J., Li, X., Huang, W., and Fan, Q. (2018). A single composition architecture-based nanoprobe for ratiometric photoacoustic imaging of glutathione (GSH) in living mice. *Small* **14**, e1703400. <https://doi.org/10.1002/smll.201703400>.
72. Kuang, Y., Liu, N., Ye, S., Li, X., Chen, X., Qi, L., Zhu, P., Liu, R., and Wu, X. (2022). Ce doped polyaniline nanoparticles for absorption and photoacoustic imaging response to GSH in vitro and in vivo. *Bioact. Mater.* **17**, 197–203. <https://doi.org/10.1016/j.bioactmat.2022.01.022>.
73. Chen, Q., Liang, C., Sun, X., Chen, J., Yang, Z., Zhao, H., Feng, L., and Liu, Z. (2017). H<sub>2</sub>O<sub>2</sub>-responsive liposomal nanoprobe for photoacoustic inflammation imaging and tumor theranostics via in vivo chromogenic assay. *Proc. Natl. Acad. Sci. USA* **114**, 5343–5348. <https://doi.org/10.1073/pnas.1701976114>.
74. Chu, C., Lin, H., Liu, H., Wang, X., Wang, J., Zhang, P., Gao, H., Huang, C., Zeng, Y., Tan, Y., et al. (2017). Tumor microenvironment-triggered supramolecular system as an in situ nanotheranostic generator for cancer phototherapy. *Adv. Mater.* **29**, 1605928. <https://doi.org/10.1002/adma.201605928>.
75. Gouda, A., Sakr, O.-S., Nasr, M., and Sammour, O. (2021). Ethanol injection technique for liposomes formulation: an insight into development, influencing factors, challenges and applications. *J. Drug Deliv. Sci. Technol.* **61**, 102174. <https://doi.org/10.1016/j.jddst.2020.102174>.
76. Hou, L., Gong, X., Yang, J., Zhang, H., Yang, W., and Chen, X. (2022). Hybrid-membrane-decorated Prussian blue for effective cancer immunotherapy via tumor-associated macrophages polarization and hypoxia relief. *Adv. Mater.* **34**, e2200389. <https://doi.org/10.1002/adma.202200389>.
77. Zhong, Y., Ma, Z., Wang, F., Wang, X., Yang, Y., Liu, Y., Zhao, X., Li, J., Du, H., Zhang, M., et al. (2019). In vivo molecular imaging for immunotherapy using ultra-bright near-infrared-IIb rare-earth nanoparticles. *Nat. Biotechnol.* **37**, 1322–1331. <https://doi.org/10.1038/s41587-019-0262-4>.
78. Wang, S., Wang, Z., Li, Z., Zhang, X., Zhang, H., Zhang, T., Meng, X., Sheng, F., and Hou, Y. (2022). Amelioration of systemic antitumor immune responses in cocktail therapy by immunomodulatory nanozymes. *Sci. Adv.* **8**, eabn3883. <https://doi.org/10.1126/sciadv.abn3883>.
79. Jacques, S.L. (2013). Optical properties of biological tissues: a review. *Phys. Med. Biol.* **58**, R37–R61. <https://doi.org/10.1088/0031-9155/58/11/r37>.
80. Li, M., Oh, J., Xie, X., Ku, G., Wang, W., Li, C., Lungu, G., Stoica, G., and Wang, L.-V. (2008). Simultaneous molecular and hypoxia imaging of brain tumors in vivo using spectroscopic photoacoustic tomography. *Proc. IEEE* **96**, 481–489. <https://doi.org/10.1109/JPROC.2007.913515>.

## STAR★METHODS

### KEY RESOURCES TABLE

REAGENT or RESOURCE	SOURCE	IDENTIFIER
<b>Chemicals, peptides, and recombinant proteins</b>		
DSPC	Xi'an RuiXi	LP-R4-076
DSPE-PEG2000	Xi'an RuiXi	LP-R4-039
[Ru(dpp) <sub>3</sub> ]Cl <sub>2</sub>	Sigma-aldrich	904767-250MG
Potassium ferrocyanide	Sinopharm Chemical Reagent	10016808
Iron tri(acetylacetonate)	Bidepharm	BD130296
<b>Critical commercial assays</b>		
Calcein-AM and propidium iodide (PI)	Bestbio	BB-4101
<b>Deposited data</b>		
Raw data	This paper	N/A
<b>Experimental models: Cell lines</b>		
Murine breast cancer 4T1 cell	ATCC	CRL-2539
Human umbilical vein endothelial cells	Wuhan Procell Life	CL-0122
<b>Experimental models: Organisms/strains</b>		
Mouse: BALB/C nude mice	Beijing Vital River	N/A
Mouse: BALB/C mice	Beijing Vital River	N/A
<b>Software and algorithms</b>		
MATLAB	Mathworks Inc.	R2020b
GraphPad Prism	GraphPad Software	Prism 9
<b>Other</b>		
TEM	JEOL	JEM-1200EX
DLS analyzer	Malvern Panalytical	Zetasizer Nano ZS90
UV–vis spectrophotometer	Techcomp	UV2300
ICP-OES	Agilent	ICPOES730
Ultrasound detector array	Imasonic	N/A
Nd:YAG laser	LOTIS	LS-2145-LT150
Infrared radiation thermal camera	FLUKE	Ti29
Dissolved oxygen meter	AZ	AZ8403
Fluorescence microscope	Leica	DMI8
Flow cytometer	FAC	SAria II

## RESOURCE AVAILABILITY

### Lead contact

Further information and requests for resources should be directed to and will be fulfilled by the lead contact, Cheng Ma ([cheng\\_ma@tsinghua.edu.cn](mailto:cheng_ma@tsinghua.edu.cn)).

### Materials availability

New unique reagents were not produced in this work.

### Data and code availability

- Data reported in this paper will be shared by the [lead contact](#) upon request.

- Matlab codes are available from the [lead contact](#) upon request.
- Any additional data supporting findings on this study are available from the [lead contact](#) upon request.

## EXPERIMENTAL MODEL AND SUBJECT DETAILS

### Animals and tumor models

BALB/C nude mice (65, female, 6-week-old) and BALB/C mice (15, female, 6-week-old) were provided by Beijing Vital River Laboratory Animal Technology Co., Ltd. All animal experiments were conducted in conformity with the regulations of the Laboratory Animal Research Center at Tsinghua University, Beijing, China. To establish subcutaneous tumors in 6-week-old female BALB/C nude mice, 4T1 cells ( $5 \times 10^7$ ) were injected subcutaneously in the backside of the mice. The liver metastasis models were developed by Beijing Medcon Biotechnology Co. Ltd. 4T1 cells ( $5 \times 10^7$ ) were injected in the right liver lobe and tumors were grown for approximately 7 days before being used for experiments.

## METHOD DETAILS

### Synthesis of ISSzyme

ISSzyme were prepared according to the standard protocol. Briefly, DSPC, DSPE-PEG2000 and Iron tri(acetylacetonate) were co-dissolved in ethanol at a molar ratio of 9:1:90 to form a lipid mixture. Then, the lipid mixture was rapidly injected into an aqueous potassium ferrocyanide solution (30 mM), followed by water bath ultrasound sonication at room temperature for 30 min. Afterward, the suspension was further homogenized by probe sonication for 5 min in an ice-water bath (Sonifier, 10% output amplitude). Then, the dialysis method was selected to remove the unencapsulated potassium ferrocyanide with a membrane of 8000–14,000 Da cut-off for 2 h at room temperature, obtaining the aqueous dispersion of ISSzyme.

### Characterization of ISSzyme

The morphology of ISSzyme was studied by TEM with an accelerating voltage of 100 kV. Briefly, the cubic grid (300 mesh) was immersed into 20  $\mu$ L of the as-prepared solution of ISSzyme for 10 min, followed by air-drying and 5 min of negative staining with 3.0% phosphotungstic acid. Then, the sample absorbed cubic grid was further washed with deionized water and air-dried for TEM observation. Data of both particle size distribution and zeta potential were tested by DLS analyzer. The absorption spectra were obtained by a UV–vis spectrophotometer.

### GSH-responsiveness of ISSzyme

ISSzyme ( $2 \text{ mg mL}^{-1}$ ) was incubated with different concentrations of GSH for 5 min. Then, the absorbances were measured by a UV–vis spectrophotometer.

### PA spectroscopic measurement

The PA spectra was measured by a home-made PACT system. A Q-switched Nd:YAG laser (532 nm) was used to pump an optical parametric oscillator to generate 680–1064 nm laser pulses. A custom-made full-ring ultrasound detector array was used to detect the PA signals. ISSzyme ( $2 \text{ mg mL}^{-1}$ ) after incubate with different concentrations of GSH were placed inside a polytetrafluoroethylene (PTFE) tube (inner diameter: 0.30 mm, outer diameter: 0.60 mm). The PTFE tubes were irradiated with wavelengths ranging from 680 to 990 nm with 10 nm increments. The peak-to-peak voltage of the PA signal was then normalized with the laser energy at each wavelength and was plotted against the wavelength to generate the PA spectra.

### Photothermal properties

ISSzyme ( $2 \text{ mg mL}^{-1}$ ) was incubated with different concentrations of GSH for 5 min. Then, all samples were exposed to laser irradiation (808 nm,  $1 \text{ W cm}^{-2}$ ) for 10 min. An infrared radiation thermal camera was used to record the temperature.

### In vitro O<sub>2</sub> generation

A dissolved oxygen meter was used to monitor the dissolved O<sub>2</sub> content in the solutions of six groups, including PBS (pH = 6.5), PBS + H<sub>2</sub>O<sub>2</sub>, GSH + H<sub>2</sub>O<sub>2</sub>, ISSzyme + GSH, ISSzyme + H<sub>2</sub>O<sub>2</sub>, ISSzyme + GSH + H<sub>2</sub>O<sub>2</sub>. For the "ISSzyme" groups, uniform concentration ( $2 \text{ mg mL}^{-1}$ ) was used. For the "GSH" groups,

uniform concentration (1 mM) was used. For the “H<sub>2</sub>O<sub>2</sub>” groups, H<sub>2</sub>O<sub>2</sub> (1 mM, 200 μL) incubated with samples at room temperature for 6 min.

### **In vitro biocompatibility of ISSzyme**

*In vitro* cytotoxicity of the ISSzyme was determined in both HUVECs and 4T1 cells by the MTT assay. HUVECs and 4T1 cells were incubated on 96-well plate for 24 h. Cells were then cultured in the medium supplemented with the indicated doses of the ISSzyme for another 24 h. Then, the biocompatibilities were evaluated by MTT assay according to the manufacturer’s protocol.

### **In vitro cytotoxicity assay of ISSzyme**

To test the PTT-induced cytotoxicity, 4T1 cells were seeded in 96 well plates and co-incubated with different concentrations of ISSzyme (GSH preincubated) for 8 h. Subsequently, Cells were irradiated by NIR laser (808 nm, 1 W cm<sup>-2</sup>) for 5 min. After washing with PBS, the cells were further cultured for 16 h. Then, the cytotoxicity was evaluated by MTT assay according to the manufacturer’s protocol. The non-irradiated cells treated with PBS were used as a control. To test the cytotoxicity induced by different irradiation conditions, uniform concentration of ISSzyme (150 μg mL<sup>-1</sup>) and various irradiation parameters (power density: 0.5, 1.0, 1.5, and 2.0 1 W cm<sup>-2</sup>, irradiation time: 0, 3, 5, and 7 min) were used. To test the cytotoxicity of ISSzyme-induced PTT, both MTT assay and Calcein-AM/PI assay were used. 4T1 cells were seeded in 96 well plates and divided into 4 groups, including control, laser (808 nm, 1 W cm<sup>-2</sup>, 5 min), ISSzyme (200 μg mL<sup>-1</sup>), and ISSzyme (200 μg mL<sup>-1</sup>) + laser (808 nm, 1 W cm<sup>-2</sup>, 5 min). After treatment, the cytotoxicity was evaluated by MTT assay according to the manufacturer’s protocol. For living and dead cell staining assay, 4T1 cells were seeded in 12 well plates and divided into 4 groups as MTT assay. The treated cells were stained with Calcein-AM and PI 30 min before fluorescence imaging. Then, an inverted fluorescence microscope was used to record the stained cells.

### **In vitro O<sub>2</sub> generation at the cellular level**

4T1 cells were seeded in 12 well plates overnight and divided into 3 groups, including control (normoxia, PBS, pH = 7.4), PBS (hypoxic, PBS, pH = 7.4), and ISSzyme (hypoxic, ISSzyme 200 μg mL<sup>-1</sup>). After 12 h, all groups were incubated with [Ru(dpp)<sub>3</sub>]Cl<sub>2</sub> (10 mg mL<sup>-1</sup>) for another 12 h. After washing with PBS to remove excess [Ru(dpp)<sub>3</sub>]Cl<sub>2</sub>, fluorescence images were recorded by an inverted fluorescence microscope.

### **In vitro invasion assay**

4T1 cells were seeded in 12 well plates overnight and divided into 3 groups, including control (normoxia, PBS, pH = 7.4), PBS (hypoxic, PBS, pH = 7.4), and ISSzyme (hypoxic, ISSzyme 200 μg mL<sup>-1</sup>). Cells in all groups were harvested and seeded in the upper chamber of the transwell system coated with 100 μL of matrigel with 10<sup>4</sup> cells per well. The RPMI 1640 in the upper chamber contained no FBS, while the RPMI 1640 in the lower chamber contained 10% FBS. After incubated for 24 h, 4T1 cells on the bottom of the polycarbonate membrane were fixed with 4% paraform and stained with 0.1% crystal violet. After washing with 3% acetic acid to remove excess crystal violet, the images were recorded by an inverted microscope.

### **In vitro apoptosis evaluation**

4T1 cells were seeded in 12 well plates and divided into 4 groups, including control, laser (808 nm, 1 W cm<sup>-2</sup>, 5 min), ISSzyme (200 μg mL<sup>-1</sup>), and ISSzyme (200 μg mL<sup>-1</sup>) + laser (808 nm, 1 W cm<sup>-2</sup>, 5 min). Apoptosis Kit with Annexin V-APC and PI was used to assess the apoptosis by flow cytometer 12 h after the treatment.

### **In vivo biocompatibility of ISSzyme**

To evaluate *in vivo* biocompatibility, ISSzyme (13 mg kg<sup>-1</sup>) were injected into 6-week-old female BALB/C nude mice through tail vein (n = 3). At 0, 1, 7, and 14 days post-injection, a blood routine examination was performed. Meanwhile, the *in vivo* biocompatibility of ISSzyme was further assessed by a histological examination. ISSzyme (13 mg kg<sup>-1</sup>) were injected into 6-week-old female BALB/C nude mice through tail vein (n = 3). At 0, 1, 7, and 14 days post-injection, major organs (heart, liver, spleen, lung, and kidney) of the mice were removed and stained with H&E.

### **In vivo biodistribution of ISSzyme**

To evaluate *in vivo* biodistribution, ISSzyme ( $13 \text{ mg kg}^{-1}$ ) were injected into 6-week-old female BALB/C nude mice through tail vein ( $n = 3$ ). At 0 to 10 days post-injection, the feces and urine of mice have been collected for ICP analysis.

### **In vivo PACT imaging**

*In vivo* PA images were recorded by a homemade PACT system. A Q-switched Nd:YAG laser, an optical parametric oscillator, and a custom-made full-ring ultrasound detector array were employed for PACT imaging. The system used was the same as in the PA spectroscopic measurement.

### **In vivo and ex vivo PAMe imaging**

A homemade PAMe system was used for recording both *in vivo* and *ex vivo* PAMe images. A high-finesse Fabry-Pérot interferometric sensor was employed as the ultrasound probe which was raster-scanned during image acquisition. Images reconstruction was subsequently performed in three dimensions. For *ex vivo* PAMe imaging, the *ex vivo* organs and tumors were fixed in 1.5% agarose after treatment with 4% paraformaldehyde fix solution before imaging.

### **In vivo thermal imaging**

6-week-old female 4T1 tumor-bearing BALB/C nude mice ( $n = 5$ ) were intravenously injected with ISSzyme ( $13 \text{ mg kg}^{-1}$ ) while mice treated with PBS were used as controls. All mice were exposed to laser irradiation ( $808 \text{ nm}$ ,  $2 \text{ W cm}^{-2}$ ) for 10 min at 10 h post-injection. An IR radiation thermal camera was used to record the thermal images and the temperature.

### **In vivo therapeutic performance of ISSzyme**

When the tumor volume reached  $\sim 100 \text{ mm}^3$ , 6-week-old female 4T1 tumor-bearing BALB/C nude mice were randomly divided into 4 groups ( $n = 5$ ), including control (PBS-treated), laser ( $808 \text{ nm}$ ,  $2 \text{ W cm}^{-2}$ , 10 min), ISSzyme ( $13 \text{ mg kg}^{-1}$ ), and ISSzyme ( $13 \text{ mg kg}^{-1}$ ) + laser ( $808 \text{ nm}$ ,  $2 \text{ W cm}^{-2}$ , 10 min). Then, the mice began to receive different treatments at days 0, 2, 4 and 6. The tumor volume of the mice was recorded and calculated every 2 days ( $V = L \cdot W^2/2$ ). Meanwhile, the body weights of all mice were also recorded. At the end of the therapeutic period, all tumors were removed, weighed and photographed.

### **Pathological investigation**

After *in vivo* treatment, tumors of all groups were collected and frozen with liquid nitrogen for histopathological analysis, including H&E staining, TUNEL assay, Ki-67 staining, and HIF- $\alpha$  staining. For the laser-treated groups, the tumor was removed after NIR irradiation. For other groups, the tumor was removed on day 6.

### **In vivo metastasis inhibition of ISSzyme**

For the metastasis inhibition study, at the end of 11 days of treatment, all of the mice were sacrificed with lungs harvested. The metastasis in the lungs of all groups were photographed and calculated to study the metastasis inhibition. Then, the lungs were fixed with 4% paraformaldehyde fix solution for H&E staining.

### **In vivo SO<sub>2</sub> monitoring**

To image the SO<sub>2</sub> distribution of the tumor, the PAMe system was employed to obtain PA images at 11 wavelengths ranging from 700 nm to 900 nm with an interval of 20 nm. The pulse-to-pulse energy was calibrated by monitoring the light energy of a reference beam split by a dielectric mirror. To calibrate the spectrum transfer function (STF) of the system, a FTFE tube (0.3 mm inner diameter) fulfilled with CuSO<sub>4</sub> solution (0.1 M) was firstly imaged by the system. With reference to the optical absorption spectrum of the CuSO<sub>4</sub> solution measured by a spectrophotometer, we calibrated the STF of the PAMe system, which was used to transfer the measured PA spectrum to the optical absorption spectrum. The standard optical absorption spectrum of oxy-hemoglobin and deoxy-hemoglobin applied in this work was obtained from a previous work.<sup>79</sup> Then the SO<sub>2</sub> was calculated using a standard linear unmixing method.<sup>80</sup> When the tumor volume reached  $\sim 100 \text{ mm}^3$ , a 6-week-old female 4T1 tumor-bearing BALB/C nude mouse was treated with ISSzyme ( $13 \text{ mg kg}^{-1}$ ). The SO<sub>2</sub> was monitored at 0 h and 10 h after treatment.

### Data processing and image reconstruction

For PACT imaging, respiratory gating was used to average 131 frames of data. PACT images were reconstructed by adopting a half-time delay-and-sum (DAS) method. For PAMe imaging, a three-dimensional DAS method was used to reconstruct the images. Hilbert transform and dual-speed-of-sound were employed during image reconstruction. All PACT and PAMe reconstructed images were rendered and displayed using MATLAB R2020b. Further image processing, including fluence compensation, image segmentation, and agent recognition, was performed in MATLAB.

### QUANTIFICATION AND STATISTICAL ANALYSIS

PA signal intensities were measured by region of interest (ROI) analysis using MATLAB. All data were presented as mean  $\pm$  standard deviation (SD). All statistical calculations were performed using GraphPad Prism 9. \*\* $p < 0.01$ , \*\*\* $p < 0.001$  and \*\*\*\* $p < 0.001$  were considered to be extremely significant.